Annu. Rev. Biophys. Biophys. Chem. 1991. 20:29–63

TWO-, THREE-, AND FOUR-DIMENSIONAL NMR METHODS FOR OBTAINING LARGER AND MORE PRECISE THREE-DIMENSIONAL STRUCTURES OF PROTEINS IN SOLUTION[1]

G. Marius Clore and Angela M. Gronenborn

Laboratory of Chemical Physics, Building 2, National Institute of Diabetes and Digestive and Kidney Diseases, National Institutes of Health, Bethesda, Maryland 20892

KEY WORDS: protein structure in solution, multidimensional NMR, nuclear Overhauser effect

CONTENTS

PERSPECTIVES AND OVERVIEW

Over the past 5 to 10 years, NMR (nuclear magnetic resonance) has developed into a powerful method for determining three-dimensional structures of small proteins of about 100 residues or less. The principal geometric information used in these structure determinations resides in short (<5 Å) approximate interproton distance restraints derived from the observation of nuclear Overhauser effects (NOE) that are proportional to r^{-6} (97). The stimulus for this rapid progress has stemmed from one technological and two methodological advances, in particular, the advent of high-field NMR spectrometers (500–600 MHz) and the development of a whole array of two-dimensional (2D) NMR experiments and of algorithms for converting NMR-derived interproton distances into cartesian coordinates. The basic strategy for NMR structure determination is relatively straightforward and can be divided into three stages: (*a*) sequential assignment of backbone and side-chain ^{1}H resonances using experiments that demonstrate through-bond (scalar) and through-space (<5 Å) connectivities; (*b*) identification of as many through-space nuclear Overhauser (NOE) connectivities as possible that yield a large set of approximate interproton-distance restraints; and (*c*) calculation of three-dimensional structures on the basis of these distance restraints, supplemented if possible by some torsion-angle restraints derived from coupling constants. The theoretical basis of two-dimensional NMR has been discussed in detail in a book by Ernst et al (47), and the application of these methods to protein structure determination has been comprehensively reviewed (5, 27, 28, 59, 115, 116).

However, several exciting developments from over the past year promise to extend the NMR methodology both with respect to the size of proteins that can be studied and to the accuracy and precision of the structure determinations. These include the extension of 2D NMR into 3D and 4D NMR and the use of systematic data-base searches to obtain numerous torsion-angle restraints on the basis of the experimental NMR data. In

this review, we outline these recent developments and illustrate their application. We show that the methodology is now at hand to determine protein structures up to ~25 kilodaltons (kd) that are comparable in quality to 2.0- to 2.5-Å-resolution X-ray structures.

PRINCIPLES OF 3D AND 4D NMR

Figure 1*A* illustrates 2D HOHAHA (homonuclear Hartman-Hahn spectroscopy) (6, 39) and NOESY (nuclear Overhauser enhancement spectroscopy) (68) spectra of interleukin-1β (IL-1β), a protein of 153 residues (42). The former contains through-bond connectivities between NH and aliphatic resonances, while the latter displays through-space (< 5 Å) connectivities between these resonances. Two features of these spectra are clearly evident. The first is the extensive overlap of resonances that renders unambiguous interpretation of cross-peaks virtually impossible in all but a few cases. The second feature is that the number of connectivities in the HOHAHA spectrum from the NH protons to the $C^{\beta}H$ protons and beyond is small. This small number results from the fact that the homonuclear J couplings that form the basis of correlation experiments [e.g. ^{1}H-^{1}H COSY (correlated spectroscopy) (2), HOHAHA, etc] are unresolved because of the relatively large linewidths of the resonances, an inevitable consequence of the longer rotational correlation time of the protein resulting from increases in the molecular weight. As a result, assignment strategies based on conventional 2D NMR experiments break down for proteins the size of IL-1β. To some extent, one can overcome this drawback by using isotope-edited 2D NMR experiments combined with selective and specific isotopic labeling (e.g. with ^{15}N) (11, 49, 56, 86, 87, 109, 110). Unfortunately, specific labeling is both expensive and technically difficult as it may require the use of auxotrophic strains and further necessitates numerous sample preparations as well as the recording of a very large number of spectra. Therefore this strategy is impractical in the majority of cases.

Problems associated with extensive chemical-shift overlap can be overcome by increasing the resolution of the spectrum. Two fundamentally different approaches lead to this higher resolution. The conventional approach attempts to improve the resolution of 2D NMR spectra by increasing the digital resolution and by using strong resolution-enhancement, digital-filtering functions at the expense of sensitivity. Unfortunately, the gain resulting from these procedures is only minimal and mostly cosmetic in nature. A new approach improves the digital resolution by increasing the dimensionality of the spectrum (74) and at the same time yields important additional information about the system (e.g. ^{15}N and ^{13}C chemical shifts in addition to ^{1}H ones). Thus, just as the increased resolu-

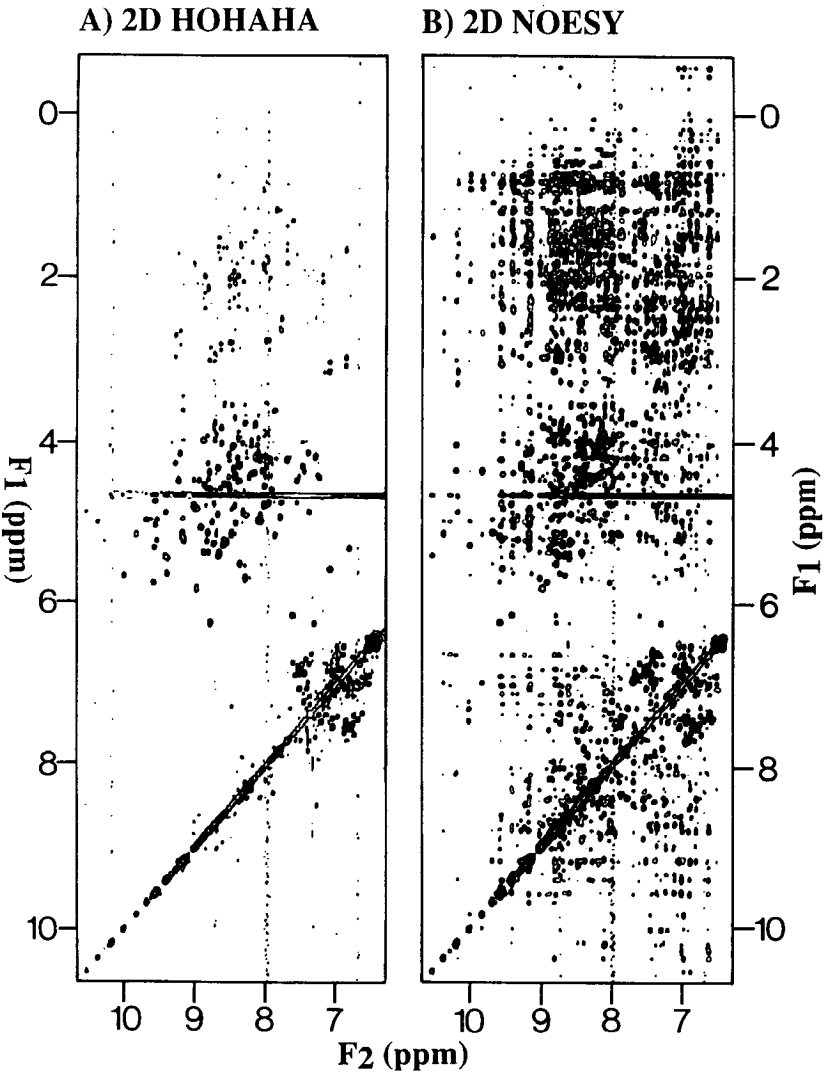

Figure 1 $F_2(NH)$-$F_1(^1H)$ region of the 600 MHz 2D ^1H-^1H HOHAHA and NOESY spectra of interleukin 1β (IL-1β). Reprinted with permission from Reference 42.

tion afforded by extending NMR experiments into a second dimension enables one to detect and interpret effects that would have been impossible to ascertain using traditional one-dimensional NMR spectroscopy, the extension into a third and even fourth dimension permits one to analyze interactions that could not have been extracted from the corresponding 2D spectra.

Figure 2 summarizes the relationship between 2D, 3D, and 4D NMR pulse sequences. All 2D experiments comprise the same basic scheme: namely a preparation pulse; an evolution period (t_1), during which the spins are labeled according to their chemical shifts; a mixing period (M), during which the spins are correlated with each other; and finally a detection period (t_2) (47). The experiment is repeated several times with successively incremented values of the evolution period t_1 to generate a data matrix $s(t_1, t_2)$. Fourier transformation of the t_2 dimension yields a set of n 1D spectra in which the intensities of the resonances are modulated sinusoidally as a function of the t_1 duration. Subsequent Fourier transformation in the t_1 dimension then yields the desired 2D frequency spectrum $S(\omega_1, \omega_2)$. A 3D pulse scheme simply combines two 2D pulse sequences, leaving out the detection period of the first and the preparation pulse of the second (55, 101). Thus, the two evolution periods, t_1 and t_2, are incremented independently, and are followed by a detection period t_3. Further extension to a fourth dimension is easily implemented by combining three 2D schemes, leaving out the preparation pulses of the second and third experiments and the detection period of the first and second (74).

The first 3D experiments to be performed on proteins were of the ^1H homonuclear variety in which a scalar correlation pulse scheme such as HOHAHA was combined with a NOESY sequence (99–101, 111, 112). While elegant, the applicability of ^1H homonuclear 3D experiments to larger proteins is limited because the efficiency of the scalar correlation step is severely reduced as line widths increase. As a result, the sensitivity of such 3D homonuclear experiments tends to be very low for proteins of $M_r > 10{,}000$. A more useful approach employs uniformly (>95%) labeled ^{15}N and/or ^{13}C proteins, thereby permitting access to the large resolved heteronuclear couplings to efficiently transfer magnetization through bonds (50, 83, 84). To this end, several heteronuclear 3D and 4D experiments have been developed, and their applications are discussed below.

2D NMR $P_a - E_a(t_1) - M_a - D_a(t_2)$

3D NMR $P_a - E_a(t_1) - M_a - E_b(t_2) - M_b - D_b(t_3)$

4D NMR $P_a - E_a(t_1) - M_a - E_b(t_2) - M_b - E_c(t_3) - M_c - D_c(t_4)$

Figure 2 Relationship between the pulse sequences for recording 2D, 3D, and 4D NMR spectra. Abbreviations are: P, preparation; E, evolution; M, mixing; and D, detection.

Figure 3 illustrates the progression and relationship between $^{15}N/^{13}C$-heteronuclear edited 2D, 3D, and 4D NOSEY experiments (74). In the 2D spectrum, one can observe NOEs between NH protons (F_2 dimension) and aliphatic protons (F_1 dimension) in a single plane. In the 3D spectrum, these NOEs are spread within a 3D cube over a series of $F_3(NH)$-$F_1(^1H)$ slices according to the chemical shift of the directly bonded ^{15}N atoms in the F_2 dimension, thus resolving ambiguities associated with NH-chemical-shift degeneracy. Ambiguities arising from severe overlap of aliphatic resonances still persist in the 3D ^{15}N-edited NOESY spectrum and can be resolved by introducing the chemical shift of the directly attached ^{13}C nuclei as the fourth dimension. Thus, in the 4D experiment, each slice at a particular ^{15}N frequency of the 3D spectrum constitutes a cube within the 4D spectrum, in which each cube is subdivided into a further series of slices based on ^{13}C chemical shift of the ^{13}C atoms directly bonded to the aliphatic protons indicated in F_1.

The pulse schemes for the various 3D and 4D spectra discussed in this review are provided in Figure 4. The 3D experiments typically take two to three days to record while the 4D ones take three to four days. High-quality 3D and 4D spectra can easily be obtained on 1- to 2-mM samples of uniformly (>95%) ^{15}N- and/or ^{13}C-labeled protein.

SEQUENTIAL ASSIGNMENT USING HETERONUCLEAR 3D NMR

The conventional sequential assignment strategy involves the use of homonuclear correlation spectroscopy to identify amino acid spin systems together with NOESY spectroscopy to identify sequential connectivities along the chain involving the NH, $C^{\alpha}H$, and $C^{\beta}H$ protons (115). β-strands usually have only strong $C^{\alpha}H(i)$-$NH(i+1)$ NOEs, supplemented by $C^{\beta}H(i)$-$NH(i+1)$ NOEs. In helices, on the other hand, consecutive stretches of $NH(i)$-$NH(i+1)$ NOEs are accompanied by $NH(i)$-$NH(i+2)$, $C^{\alpha}H(i)$-$NH(i+1, 2, 3, 4)$, $C^{\beta}H(i)$-$NH(i+1)$, and $C^{\alpha}H(i)$-$C^{\beta}H(i+3)$ NOEs. The same strategy can be used in 3D NMR (42, 45, 83). In addition, however, triple resonance experiments involving correlations of ^1H, ^{13}C, and ^{15}N chemical shifts can provide sequential connectivities by means of heteronuclear through-bond couplings (65, 76).

Assignment of Spin Systems

In homonuclear ^1H NMR, spin systems are usually assigned by means of COSY (2) spectra to identify direct through-bond connectivities in conjunction with HOHAHA (6, 39) spectra to identify multiple relayed

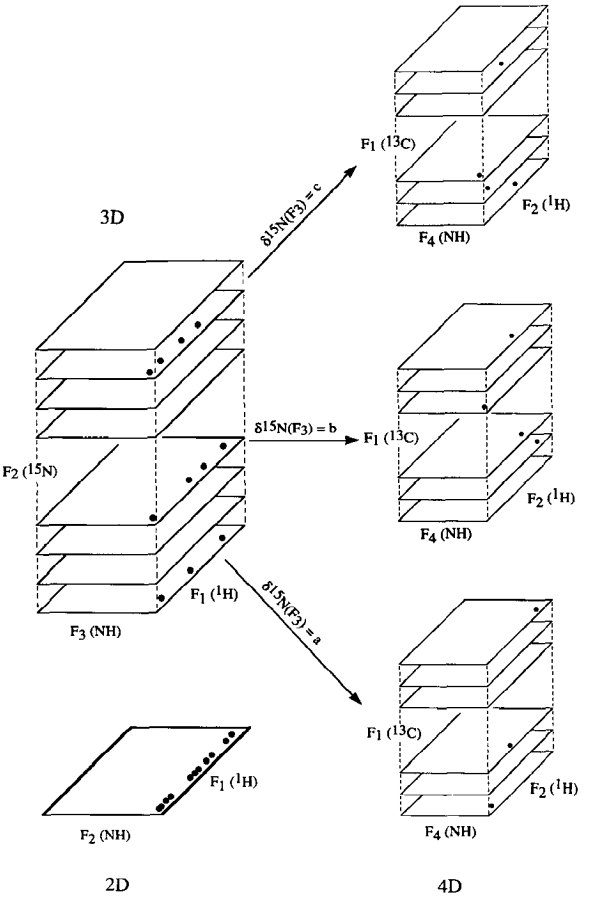

Figure 3 Schematic illustration of the progression and relationship between heteronuclear $^{15}N/^{13}C$-edited 2D, 3D, and 4D NOESY spectra. The *closed circles* represent NOE cross peaks between NH and aliphatic protons. In the 2D spectrum, cross peaks from 11 aliphatic protons to three NH protons at a single NH chemical shift are indicated. In the 3D spectrum, these peaks are spread into a third dimension according to the chemical shift of the directly bonded ^{15}N atoms, and in the figure the peaks are now distributed in three distinct ^{15}N planes, thereby removing the overlap associated with NH-chemical-shift degeneracy. The identity of the aliphatic protons, however, can still only be established on the basis of their ^{1}H chemical shifts. In the 4D spectrum, each ^{15}N plane of the 3D spectrum constitutes a cube composed of a series of slices at different ^{13}C chemical shifts. The identity of the originating aliphatic protons can now be established unambiguously on the basis of their ^{1}H and ^{13}C chemical shifts. Reprinted with permission from Reference 74.

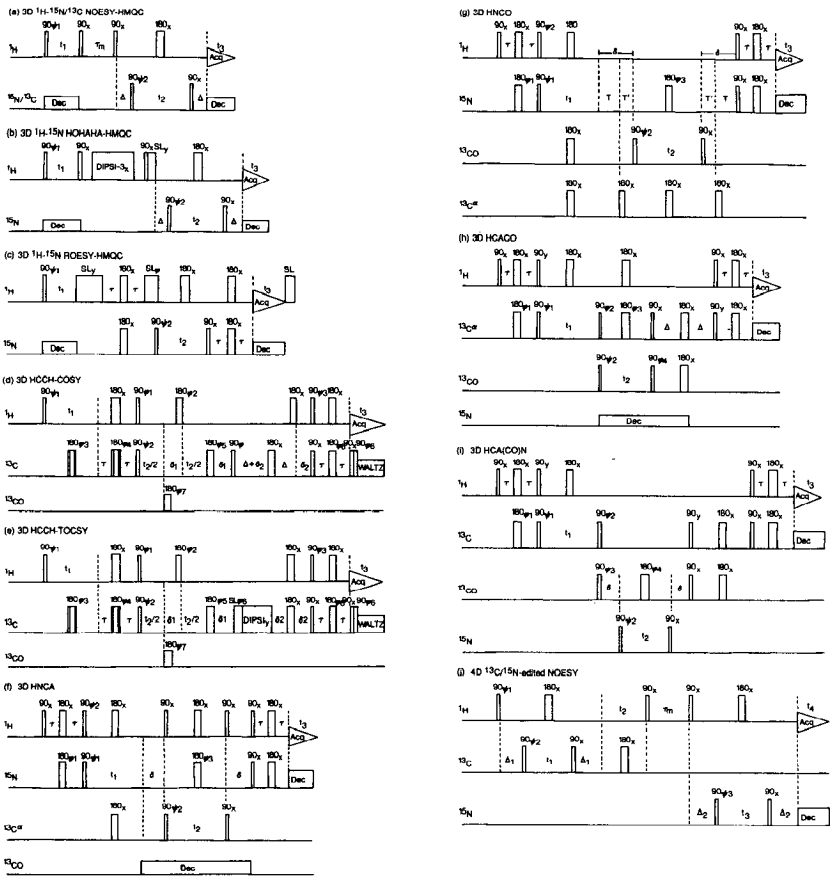

Figure 4 Pulse schemes for the most useful heteronuclear 3D and 4D NMR experiments. (*a*) 3D ^{1}H-^{15}N or ^{1}H-^{13}C NOESY-HMQC; (*b*) 3D ^{1}H-^{15}N HOHAHA-HMQC; (*c*) 3D ^{1}H-^{15}N ROESY-HMQC; (*d*) 3D HCCH-COSY; (*e*) 3D HCCH-TOCSY; (*f*) 3D HNCA; (*g*) 3D HNCO; (*h*) 3D HCACO; (*i*) 3D HCA(CO)N; (*j*) 4D ^{13}C/^{15}N edited NOESY. Phases indicated by ψ must be appropriately incremented to obtain quadrature in the t_1 and t_2 dimensions, and, in the 4D experiment, in the t_3 dimension as well.

connectivities along the side chain. Connectivities from the NH protons to the C$^{\alpha}$H protons are obtained from a spectrum recorded in water, while connectivities between the aliphatic protons are observed in a spectrum recorded in D_2O. For larger proteins, the sensitivity of homonuclear J correlation experiments is severely reduced because of the slow tumbling of the large proteins that results in ^{1}H linewidths that are often significantly

larger than many of the ^{1}H-^{1}H couplings (42). This problem can be circumvented by resorting to techniques that do not rely on the poorly resolved ^{1}H-^{1}H couplings to establish through-bond connectivities but instead utilize the well-resolved one-bond ^{1}H-^{13}C, ^{13}C-^{13}C, ^{1}H-^{15}N, and ^{15}N-$^{13}C^{\alpha}$ J couplings to transfer magnetization (7, 8, 22, 48, 65, 75, 76).

The strategy to identify spin systems using heteronuclear 3D NMR comprises two stages (22). In the first step, the NH and ^{15}N chemical shifts of each residue are correlated with the corresponding $^{13}C^{\alpha}$ and $C^{\alpha}H$ proton chemical shifts using 3D ^{1}H-^{15}N HOHAHA-HMQC (heteronuclear multiple quantum coherence spectroscopy) (83) (Figure 4*b*) and triple resonance ^{1}H-^{15}N-$^{13}C^{\alpha}$ (HNCA) (76) (Figure 4*f*) spectroscopy, respectively. The first experiment relies on transfer of magnetization between NH and $C^{\alpha}H$ spins via the three-bond homonuclear intraresidue $^{3}J_{HN\alpha}$ coupling, while the second involves transfer of magnetization via the one-bond heteronuclear $^{1}J_{NC\alpha}$ intraresidue coupling. In the HOHAHA-HMQC experiment (Figure 4*b*), aliphatic ^{1}H chemical shifts evolve during the period t_1. Transfer of magnetization originating on aliphatic protons to the corresponding intraresidue NH protons is achieved via isotropic mixing of ^{1}H magnetization. Magnetization, which now resides on the NH protons, is transferred to the directly bonded ^{15}N spins by means of multiple quantum coherence (10, 89, 107). ^{15}N chemical shifts evolve during the period t_2. Magnetization is then transferred back from the ^{15}N spins to the directly bonded NH protons via multiple quantum coherence and detected during the acquisition period t_3. The HNCA experiment (Figure 4*f*), on the other hand, allows the researcher to transfer magnetization originating on an NH proton to its directly bonded ^{15}N spin via an INEPT sequence. This transfer is followed by the evolution of ^{15}N chemical shifts during the period t_1; subsequent application of 90° pulses to both ^{1}H and $^{13}C^{\alpha}$ spins establishes three-spin NH-^{15}N-$^{13}C^{\alpha}$ coherence, and $^{13}C^{\alpha}$ chemical shifts evolve during the period t_2. Magnetization is then transferred back to the NH protons by simply reversing the above procedure. Figures 5 and 6 show examples of slices of the ^{1}H-^{15}N HOHAHA-HMQC and HNCA spectra of ^{15}N- and $^{15}N/^{13}C$-labeled IL-1β at different ^{15}N frequencies. The 3D ^{1}H-^{15}N HOHAHA-HMQC spectrum appears as a regular 2D ^{1}H-^{1}H HOHAHA spectrum except, of course, that the peaks are spread out over a series of slices edited by the ^{15}N chemical shifts. Similarly, the HNCA spectrum looks like a 2D ^{1}H-^{13}C correlation spectrum, with the peaks once again spread out in a third dimension according to the ^{15}N chemical shifts. The simplicity of the spectra renders their interpretation straightforward. Both types of spectra must be recorded to correlate the $C^{\alpha}H$ and $^{13}C^{\alpha}$ chemical shifts of a given residue unambiguously because for larger proteins with many degenerate $C^{\alpha}H$ chemical shifts, the $^{13}C^{\alpha}$ chemical shifts

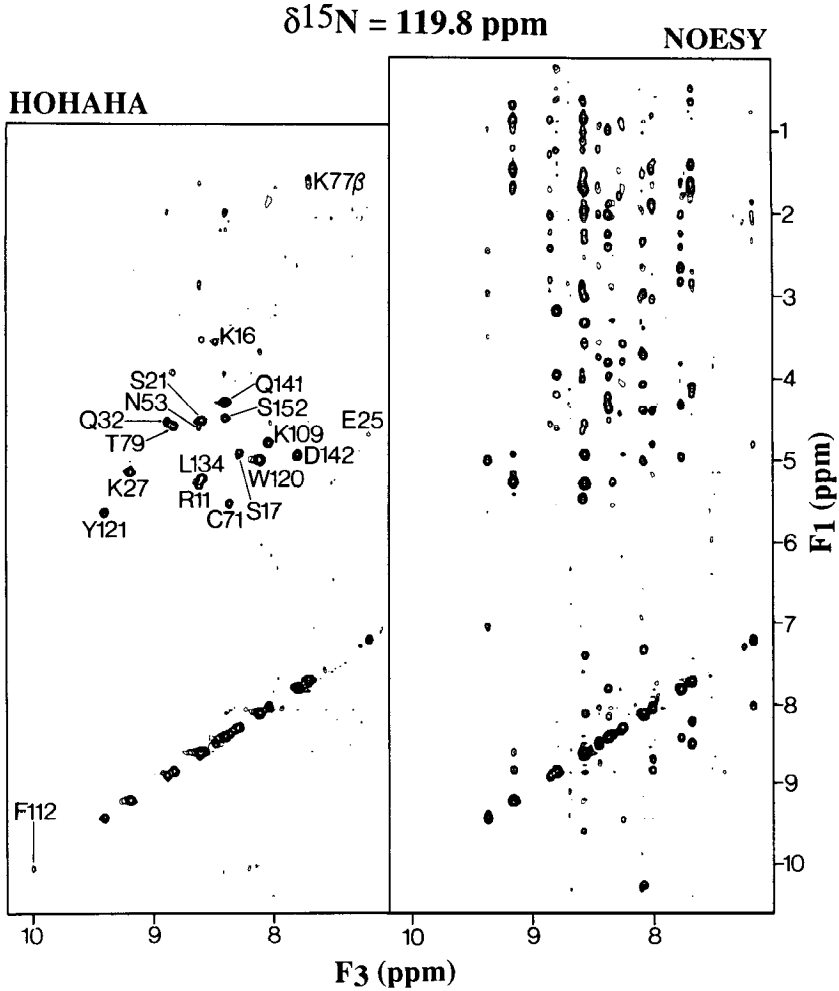

Figure 5 Representative NH(F_3)-^{1}H(F_1) planes at one ^{15}N(F_2) frequency of the 3D ^{1}H-^{15}N HOHAHA-HMQC and ^{1}H-^{15}N NOESY-HMQC spectra of ^{15}N-labeled IL-1β. Reprinted with permission from Reference 42.

cannot simply be determined by recording a 2D ^{1}H-^{13}C-shift correlation spectrum.

The amino acid spin systems can be delineated using the HCCH-COSY (^{1}H-^{13}C-^{13}C-^{1}H correlated spectroscopy) (7, 75) (Figure 4*d*) and HCCH-TOCSY (^{1}H-^{13}C-^{13}C-^{1}H total correlated spectroscopy) (8) (Figure 4*e*) experiments once the C$^\alpha$H and ^{13}C$^\alpha$ resonances of each residue have been correlated. Both experiments are based on analogous principles and use

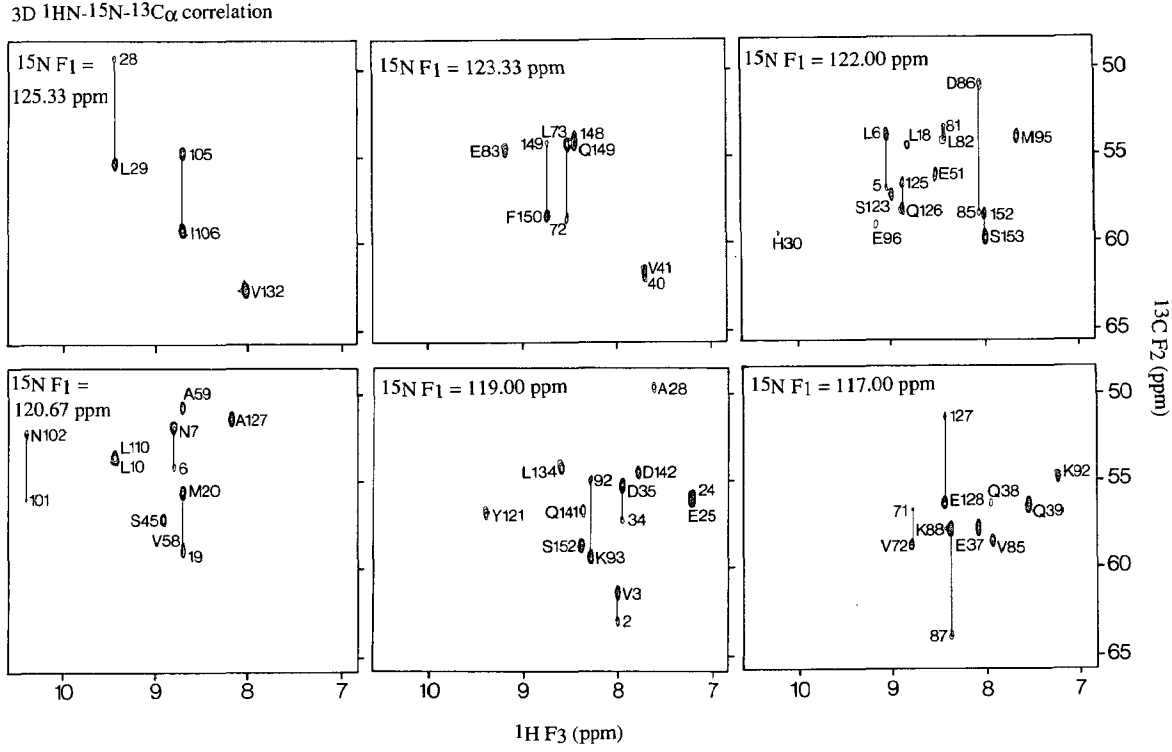

Figure 6 Representative NH(F_3)-^{13}C(F_2) planes at different ^{15}N(F_1) frequencies of the 3D HNCA spectrum of uniformly ^{15}N/^{13}C-labeled IL-1β. The intraresidue NH(i)-^{15}N(i)-^{13}C$^{\alpha}$(i) correlations are indicated by the residue name and number, while the weaker interresidue (NH(i)-^{15}N(i)-^{13}C$^{\alpha}$($i-1$) cross peaks are indicated by residue number only. Reprinted with permission from Reference 22.

the well-resolved one-bond ^{1}H-^{13}C ($\sim$140 Hz) and ^{13}C-^{13}C (30–40 Hz) J couplings to transfer magnetization, thereby circumventing the problems associated with conventional methodologies (e.g. ^{1}H-^{1}H COSY, HOHAHA, etc) that rely on poorly resolved ^{1}H-^{1}H couplings (3–12 Hz). The pulse scheme for the two experiments is comparable (Figure 4*d*, *e*). In the first step, ^{1}H magnetization from a proton is transferred to its directly bonded ^{13}C nucleus via the $^1J_{CH}$ coupling in an INEPT manner. In the second step, ^{13}C magnetization is transferred to its ^{13}C neighbor(s) via the $^1J_{CC}$ coupling. In the HCCH-COSY experiment, transfer is achieved by a 90° ^{13}C COSY mixing pulse so that magnetization is transferred only from a ^{13}C nucleus to its directly bonded ^{13}C neighbors; in the HCCH-TOCSY experiment, isotropic mixing of ^{13}C spins results in both direct and multiple-relayed magnetization transfers along the carbon chain. Ultimately, ^{13}C magnetization is transferred back to ^{1}H via the $^1J_{CH}$ coupling and detected during t_3. The final result is a 3D spectrum in which each ^{1}H(F_1)-^{1}H(F_3) plane appears similar to one from a 2D ^{1}H-^{1}H COSY or HOHAHA/TOCSY experiment but is edited by the ^{13}C chemical shift of the ^{13}C nucleus directly bonded to the ^{1}H at the diagonal position from which the magnetization originates. Further, in contrast to the 2D correlation experiments, the cross peaks in each plane do not occur symmetrically on either side of the diagonal. Consider the case in which magnetization is transferred from proton A to proton B. In the plane corresponding to the ^{13}C chemical shift of the ^{13}C nucleus directly bonded to proton A where magnetization originates, a correlation is observed between the diagonal peak at $(F_1, F_3) = (\delta_A, \delta_B)$ and a cross peak at $(F_1, F_3) = (\delta_A, \delta_B)$ in one half of the spectrum. The symmetric correlation between the diagonal peak at $(F_1, F_3) = (\delta_B, \delta_B)$ and the cross-peak at $(F_1, F_3) = (\delta_B, \delta_A)$ is then seen in the plane corresponding to the ^{13}C chemical shift of the ^{13}C nucleus directly bonded to proton B. By this means each step of the process provides unambiguous checks on the assignments. This procedure is relatively straightforward because the ^{13}C chemical shifts for different carbon types are located in characteristic regions of the ^{13}C spectrum with little overlap. Figure 7 shows examples of ^{1}H(F_3)-^{1}H(F_1) planes at a selected ^{13}C(F_2) frequency from the HCCH-COSY and HCCH-TOCSY spectrum of ^{15}N/^{13}C-labeled IL-1β (22). The HCCH-COSY experiment is particularly useful for identifying Gly, Ala, Thr, Val, and AMX spin systems, while the HCCH-TOCSY experiment is ideally suited to longer side chains. Delineation of complete Lys, Leu, Arg, and Pro spin systems from the HCCH-TOCSY spectrum is easy compared with conventional ^{1}H-^{1}H spectroscopy because, even for smaller proteins of 50–80 residues, the ratios of linewidths to ^{1}H-^{1}H three-bond couplings are unfavorable for efficient magnetization transfer.

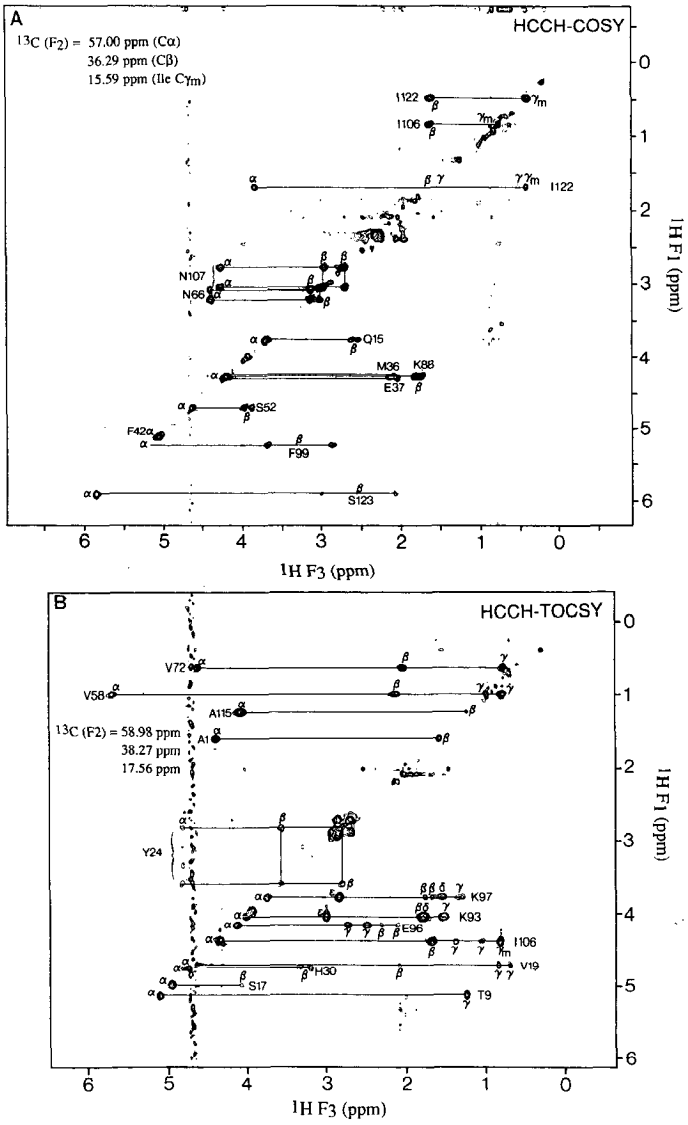

Figure 7 Representative $^{1}H(F_3)$-$^{1}H(F_1)$ slice at a selected $^{13}C(F_2)$ frequency of the 3D HCCH-COSY (*A*) and HCCH-TOCSY (*B*) spectra of uniformly $^{15}N/^{13}C$-labeled IL-1β. Reprinted with permission from Reference 22.

The success and practical applicability of these 3D techniques is demonstrated by the results on IL-1β, a protein of 153 residues (17.4 kd). Complete ^{1}H, ^{15}N, and ^{13}C resonance assignments were obtained using the 3D HNCA, HCCH-COSY, and HCCH-TOCSY experiments described above (22).

Conventional Sequential Assignment Using 3D NMR

As pointed out above, conventional sequential assignment relies on identifying NOE connectivities between adjacent residues involving the NH, $C^{\alpha}H$, and $C^{\beta}H$ protons. The same approach can be used in 3D NMR, using the 3D ^{1}H-^{15}N HOHAHA-HMQC spectrum described above to identify intraresidue connectivities between NH and $C^{\alpha}H$ protons and the 3D ^{1}H-^{15}N NOESY-HMQC spectrum to identify through-space connectivities (83). This procedure has been used to obtain complete sequential assignments of the polypeptide backbone of IL-1β (153 residues, 17.4 kd) (42). The two experiments are similar, differing only in the mixing sequence (HOHAHA versus NOE mixing; cf. Figures 4*a*, *b*). Thus, the 3D ^{1}H-^{15}N NOESY-HMQC spectrum appears the same as the $F_2(NH)$-$F_2(^{1}H)$ region of a conventional ^{1}H-^{1}H NOESY spectrum, spread out in a series of slices according to the ^{15}N chemical shifts (50, 77, 83, 84, 118). One can then proceed with sequential assignments in a relatively straightforward manner by hopping from one pair of HOHAHA/NOESY planes to another pair, connecting them via either $C^{\alpha}H(i)$-$NH(i+1)$ or $NH(i)$-$NH(i+1)$ NOEs in a manner analogous to that employed in the analysis of 2D spectra (83). For an alternative method of analysis, one can select strips of data from each slice containing cross-peaks arising from each amide NH group, thereby eliminating the empty space present in the 3D spectrum and the redundancy caused by the fact that a series of cross peaks from a single amide NH may appear in more than one slice of the 3D spectrum (42). In this manner, all the information present in the 3D ^{1}H-^{15}N NOESY-HMQC spectrum can be reduced to a relatively small number of 2D plots. Initially, the ordering of strips is purely arbitrary, but the strips can be reordered to be consistent with the amino acid sequence after the completion of the sequential assignment process, as illustrated in Figure 8.

Sequential Assignment Via Well-Resolved One-Bond J Couplings

In addition to the conventional sequential assignment approach that relies on the use of the NOE, 3D NMR also permits one to use triple resonance experiments to sequentially assign the backbone NH, ^{15}N, $^{13}C^{\alpha}$, ^{13}CO, and $C^{\alpha}H$ resonances by means of heteronuclear one-bond couplings without any need for a knowledge of spin systems (65, 76). This approach relies

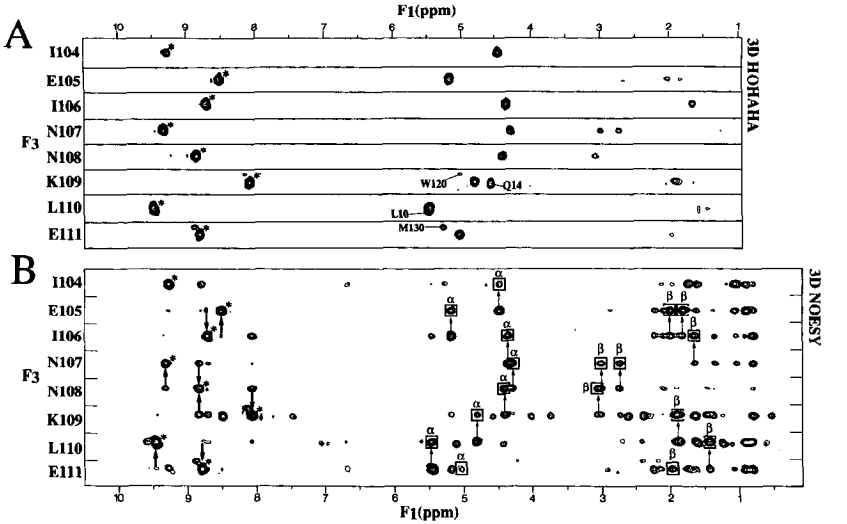

Figure 8 Illustration of sequential assignment in ^{15}N-labeled IL-1β using 3D ^{1}H-^{15}N NOESY-HMQC and HOHAHA-HMQC spectra in which the empty space present in the 3D spectra has been eliminated and the relevant data from each ^{15}N slice has been extracted in the form of strips displayed in the form of a 2D plot. The "diagonal" NH peaks are indicated by *asterisks* and NH-NH and NH-C$^{\alpha}$H and NH-C$^{\beta}$H cross-peaks for residues Ile-104 through Glu-111 are shown. Reprinted with permission from Reference 42.

on five 3D experiments, two of which, the ^{1}H-^{15}N HOHAHA-HMQC and the HNCA experiment, are described above with respect to spin system identification. The other three experiments are the 3D HNCO (NH-^{15}N-^{13}CO), HCACO (C$^{\alpha}$H-^{13}C$^{\alpha}$-^{13}CO), and HCA(CO)N (C$^{\alpha}$H-^{13}C$^{\alpha}$-^{15}N correlation spectroscopy relayed via ^{13}CO) experiments (65, 76) (Figures 4*g–i*).

The HNCO experiment (65, 76) (Figure 4*g*) correlates the NH and ^{15}N chemical shifts of residue *i* with the ^{13}CO shift of the preceding residue via the one-bond $^{1}J_{NCO}$ coupling ($\sim$15 Hz), thereby providing sequential connectivity information. In this experiment, magnetization originating from NH protons is transferred to the directly bonded ^{15}N spins using an INEPT sequence, after which ^{15}N magnetization evolves exclusively under the influence of the ^{15}N chemical shift. During the delay δ, ^{15}N magnetization becomes antiphase with respect to the polarization of the carbonyl spin of the preceding residue via the $^{1}J_{NCO}$ coupling, and the subsequent 90° ^{13}CO pulse converts this magnetization into ^{15}N-^{13}CO two-spin coherence. Evolution of ^{13}CO chemical shifts then occurs during the period t_2, and magnetization is finally transferred back to the NH protons by reversing the transfer steps. The magnetization is detected during t_3.

The HCACO experiment (65, 76) (Figure 4*h*) correlates the intraresidue $C^{\alpha}H$, $^{13}C^{\alpha}$, and ^{13}CO shifts. Magnetization is transferred from $C^{\alpha}H$ protons to the directly bonded $^{13}C^{\alpha}$ spins via an INEPT sequence, and $^{13}C^{\alpha}$ magnetization evolves during the period t_1 under the influence of the $^{13}C^{\alpha}$ chemical shift as well as the $^{13}C^{\alpha}$-^{13}CO and $^{13}C^{\alpha}$-$^{13}C^{\beta}$ J couplings. Transfer of magnetization occurs next in a COSY-like manner from $^{13}C^{\alpha}$ spins to ^{13}CO spins via the $^{1}J_{C^{\alpha}CO}$ coupling through the application of simultaneous 90° $^{13}C^{\alpha}$ and ^{13}CO pulses. Evolution of ^{13}CO chemical shifts occurs during t_2, and ^{13}CO magnetization is then transferred back to $^{13}C^{\alpha}$ by the application of simultaneous $^{13}C^{\alpha}$ and ^{13}CO pulses. At this point, the $^{13}C^{\alpha}$ magnetization is anti-phase with respect to the ^{13}CO spin state. This antiphase magnetization is removed during the subsequent interval 2Δ, and finally magnetization is transferred all the way back to the $C^{\alpha}H$ spins by a reverse-INEPT sequence and detected during t_3.

The HCA(CO)N experiment (65, 76) (Figure 4*i*) provides a second source of sequential information by correlating the $C^{\alpha}H$ and $^{13}C^{\alpha}$ shifts of residue i with the ^{15}N shift of residue $i+1$. The experiment is very similar to the HCACO one, except that magnetization transferred to the ^{13}CO spin in the HCACO experiment is subsequently transferred to the ^{15}N spin of residue $i+1$. This transfer is achieved by simply including an interval $\delta \sim 0.3/J_{NCO}$ (18 ms) after the end of the t_1 period so that the ^{13}CO magnetization becomes antiphase with respect to that of the directly bonded ^{15}N spin. The subsequent ^{15}N 90° pulse generates two-spin ^{15}N-^{13}CO coherence that evolves during t_2 under the influence of the ^{15}N chemical shift only. At the end of the t_2 period, magnetization is transferred back to the $C^{\alpha}H$ protons by reversing the transfer steps and detected during t_3.

Finally, the HNCA experiment offers a third sequential connectivity pathway (65, 76), which, in addition to the intraresidue NH(i)-^{15}N(i)-$^{13}C^{\alpha}(i)$ correlations, may reveal several weaker interresidue NH(i)-^{15}N(i)-$^{13}C^{\alpha}(i-1)$ correlations that arise via the small (≤ 7 Hz) two-bond $^{2}J_{NC\alpha}$ interresidue coupling (e.g. see Figure 5).

IDENTIFICATION OF LONG RANGE NOE CONNECTIVITIES BY HETERONUCLEAR 3D AND 4D NMR

The key to determining the protein fold lies in the identification of NOEs between residues far apart in the sequence but close together in space. This step can only be accomplished once complete (or almost complete) resonance assignments are available from the methods described earlier. Often, particularly for larger proteins, the assignments of many tertiary NOE cross peaks in conventional 2D ^{1}H-^{1}H NOESY spectra are ambigu-

ous because of severe resonance overlap. One can resolve this problem by applying 3D and 4D heteronuclear edited NOESY spectroscopy.

NOEs Between Nonexchangeable Protons

Ambiguities in nonexchangeable protons (which are invariably attached to carbon atoms) that arise from ^{1}H chemical shift overlap can be resolved by recording a 3D ^{13}C-^{1}H NOESY-HMQC spectrum (Figure 4*a*) in which NOEs between the protons are spread out according to the chemical shift of the ^{13}C spin directly bonded to the originating proton (66, 119). Just as in the HCCH-COSY and HCCH-TOCSY 3D spectra described above, the spectrum at each ^{13}C slice of the 3D ^{1}H-^{13}C NOESY-HMQC is asymmetric around the diagonal. Thus, a NOE originating on proton A and ending on proton B appears in the ^{13}C slice corresponding to the ^{13}C spin attached to proton A, while the corresponding NOE from proton B to proton A appears in the ^{13}C slice corresponding to the ^{13}C spin attached to proton B. However, there is still a significant amount of spectral overlap in the 3D ^{13}C-edited NOESY spectrum that precludes its complete interpretation. A better approach is to extend the dimensionality further and record a 4D $^{13}C/^{13}C$-edited NOESY spectrum analogous to the 4D $^{15}N/^{13}C$-edited experiment described below.

NOEs Involving Protons Attached to Nitrogen

In the 3D ^{1}H-^{15}N NOESY-HMQC experiment, the chemical shift of the directly bonded ^{15}N atoms spreads the NOEs between NH protons and aliphatic protons into a third dimension. Although, as discussed above, this 3D experiment effectively removes almost all chemical-shift degeneracy associated with the NH protons, it does not affect ambiguities associated with severe overlap of the aliphatic protons. Thus, even if a cross peak connecting an aliphatic and amide proton is well resolved in the 3D spectrum, often one cannot conclusively identify the aliphatic proton involved on the basis of its ^{1}H chemical shift, except in cases involving the $C^{\alpha}H$ resonances. One may overcome this problem by introducing a fourth dimension comprising the ^{13}C chemical shift of ^{13}C spins directly bonded to the aliphatic protons (74). This $^{15}N/^{13}C$-edited experiment (Figure 4*j*) combines three separate 2D experiments, namely ^{1}H-^{13}C HMQC, ^{1}H-^{1}H NOESY, and ^{1}H-^{15}N HMQC sequences. Multiple quantum coherence enables the transfer of magnetization between protons and the directly bonded ^{15}N or ^{13}C heteronucleus, while transfer between protons occurs via through-space NOE effects. The chemical shifts of ^{13}C, ^{1}H, and ^{15}N evolve during the variable time periods t_1, t_2, and t_3, which are incremented independently, and the NH signal is acquired during the acquisition period t_4. There are three key aspects to this 4D experiment. First, the number of peaks in the 4D spectrum is the same as that present in the corresponding

$^{15}N/^{13}C$-edited 3D and 2D spectra, so that the extension to a fourth dimension increases the resolution without a concomitant increase in complexity. Second, the through-bond transfer steps are highly efficient because they involve one-bond heteronuclear couplings (90–130 Hz) that are much larger than the linewidths. As a result, the sensitivity of the experiment is high and can easily be performed on a 1- to 2-mM sample of uniformly labeled $^{15}N/^{13}C$ protein. Third, extensive folding can be employed to maximize resolution in the $^{13}C(F_1)$ dimension so that each ^{13}C coordinate corresponds to a series of ^{13}C chemical shifts separated by intervals of approximately 20 ppm. Folding does not complicate the interpretation of the 4D spectrum because all ^{13}C resonances would have been previously assigned using the 3D HNCA, HCCH-COSY, and HCCH-TOCSY experiments described above, and the appropriate ^{13}C chemical shift is easily ascertained on the basis of the ^{1}H chemical shift of the aliphatic proton from which the magnetization originates.

Figure 9 shows selected $F_4(NH)$-$F_2(^{1}H)$ slices of the 4D $^{15}N/^{13}C$-edited NOESY experiment on $^{15}N/^{13}C$-labeled IL-1β at two $^{15}N(F_3)$ and several $^{13}C(F_1)$ frequencies, together with the corresponding $F_3(NH)$-$F_1(^{1}H)$ slices of the 3D $^{15}N/^{13}C$-edited ^{1}H-^{15}N NOESY-HMQC spectrum at the same $^{15}N(F_2)$ chemical shifts (74). Clearly, the resolution relative to the 3D spectrum is improved.

Such 4D experiments will be extremely useful for the computer-automated assignment of long range NOEs.

STEREOSPECIFIC ASSIGNMENTS AND TORSION ANGLE RESTRAINTS

The early NMR structures were generally obtained by treating NOEs involving chiral protons (e.g. β-methylene protons) as a single distance restraint referred to a center-average position of the chiral protons (35, 117). In addition, torsion-angle restraints, if there were any, were restricted to ϕ backbone torsion angles, classified into two ranges, $-35° < \phi < -85°$ and $-80° < \phi < -175°$, corresponding to $^{3}J_{HN\alpha}$ coupling constants smaller than 6 Hz and larger than 8 Hz, respectively, on the basis of an empirical Karplus equation (70, 104). The resulting structures, which on average were calculated with about seven experimental restraints per amino acid, generally exhibited atomic root mean square (rms) distributions about the mean coordinate positions of 1–2 Å for the backbone atoms and 1.5–3.0 Å for all atoms (27, 115). Both the backbone and the detailed side chain arrangements can be improved using stereospecific assignments of β-methylene protons and other chiral groups and introducing many ϕ and ψ backbone and χ_1 side-chain torsion angles, thereby

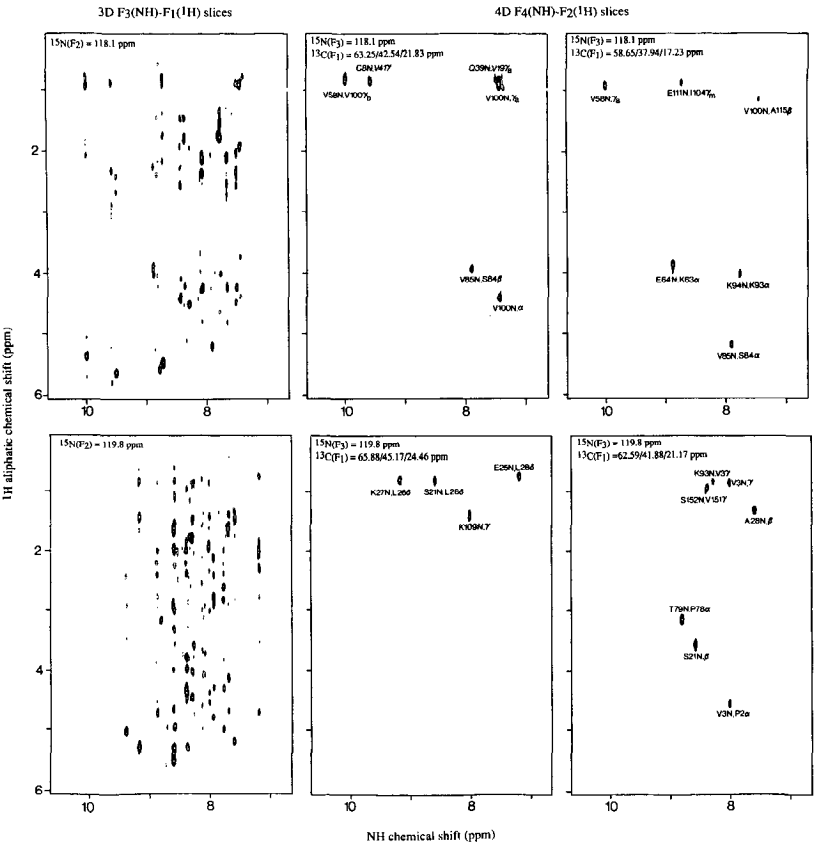

Figure 9 Representative $F_4(NH)$-$F_2(^1H)$ planes of the 4D $^{15}N/^{13}C$-edited NOESY spectrum of $^{15}N/^{13}C$-labeled IL-1β together with the $F_3(NH)$-$F_1(^1H)$ slices of the 3D $^{15}N/^{13}C$-edited spectrum at the corresponding ^{15}N frequencies. Reprinted with permission from Reference 74.

increasing the number of experimental restraints to approximately 15 per amino acid (44, 60, 94). In this section, we outline the experimental techniques required to accurately measure the $^3J_{HN\alpha}$ and $^3J_{\alpha\beta}$ coupling constants related to the torsion angles ϕ and χ_1 via empirical Karplus equations and methods for determining stereospecific assignments and torsion-angle restraints.

Measurement of $^3J_{HN\alpha}$ and $^3J_{\alpha\beta}$ Coupling Constants

Conventionally, $^3J_{HN\alpha}$ coupling constants have been measured from the peak-to-peak separation of the antiphase components of the NH-C$^\alpha$H

cross peaks in a ^{1}H-^{1}H COSY spectrum (91). A fundamental limitation of this approach is that the minimum separation of the antiphase components of the cross peaks is approximately half the NH linewidth (91). For proteins weighing 10–20 kd, the NH linewidths are typically 10–25 Hz, making impossible measurements of many of the couplings, particularly those in α-helices that normally lie between 3 and 6 Hz. An alternative approach that allows one to obtain highly accurate $^3J_{HN\alpha}$ coupling constants for proteins up to at least 25 kd uses ^{15}N uniformly labeled protein and relies on the favorable relaxation properties of ^{15}N-^{1}H zero and double quantum coherences, which result in significantly narrower multiple quantum linewidths in the F_1 dimension of an ^{1}H-^{15}N HMQC-J spectrum compared with the regular NH ^{1}H linewidths in the F_2 dimension of a ^{1}H-^{1}H-COSY spectrum (57, 72). Experience with three proteins, human thioredoxin (105 residues) (53), Staphylococcal nuclease (149 residues) (73), and IL-1β (153 residues) (45) indicates that couplings as small as 3 Hz can be reliably determined within an accuracy of ± 0.5 Hz for proteins of 15–20 kd.

The measurement of $^3J_{\alpha\beta}$ couplings from a ^{1}H-^{1}H COSY spectrum suffers from exactly the same problem as that described above for the $^3J_{HN\alpha}$ couplings. Experiments to overcome this limitation, such as β-COSY (9), E.COSY (exclusive COSY) (54), PE.COSY (primitive exclusive COSY) (82, 90), or z-COSY (102), are aimed at obtaining reduced multiplet cross-peak patterns. With the exception of the PE.COSY experiment, all these experiments still have several serious drawbacks with regard to their practical application. The β-COSY experiment suffers from a dispersive lineshape of the diagonal so that measuring splittings from cross peaks close to the diagonal is difficult. The E.COSY experiment exhibits very low sensitivity, while the z-COSY spectrum displays many zero quantum transition peaks that may obscure the correlation peaks. In our experience, the PE.COSY experiment, a variant of the β-COSY experiment in which the dispersive character of the diagonal is purged by subtracting a 0°–mixing pulse COSY spectrum from a 35°–mixing pulse COSY spectrum, is at least four times more sensitive than an E.COSY experiment (80, 82, 90).

For larger proteins, measurement of $^3J_{\alpha\beta}$ couplings from a 2D ^{1}H-^{1}H PE.COSY spectrum is likely to be difficult for the majority of residues because of extensive resonance overlap. In such cases, a qualitative estimation of the relative values of the $^3J_{\alpha\beta}$ coupling constants can potentially be obtained from the relative intensities of the NH-C$^\beta$H cross peaks in a 3D ^{1}H-^{15}N HOHAHA-HMQC spectrum because the extent of magnetization transfer from the NH to the C$^\beta$H protons during the Hartmann-Hahn mixing process depends on the magnitude of the $^3J_{\alpha\beta}$ coupling constants

(5). For small values of $^3J_{\alpha\beta}$ (i.e. <4 Hz), cross peaks will be weak or absent, whereas, for large values of $^3J_{\alpha\beta}$, sizeable cross peaks should be observed. As is discussed below, this information alone is often sufficient for the purposes of stereospecific assignment.

Conformational Data-Base Searches for Stereospecific Assignments and Torsion-Angle Restraints

Stereospecific assignments can often be obtained from a qualitative analysis of the $^3J_{\alpha\beta}$ coupling-constants data and intraresidue NOEs from the NH and $C^\alpha H$ protons to the $C^\beta H$ protons. The $^3J_{\alpha\beta}$ coupling constants are related to the χ_1 torsion angle via two empirical Karplus equations (41). If both $^3J_{\alpha\beta}$ couplings are small (~ 3 Hz), then χ_1 must lie in the range $60 \pm 60°$. If, on the other hand, one of the $^3J_{\alpha\beta}$ couplings is large (>10 Hz), the other must be small (<4 Hz), and χ_1 lies either in the range $180 \pm 60°$ or $-60 \pm 60°$ (113). These latter two possibilities are easily distinguished by short-mixing-time NOESY experiments that simultaneously yield stereospecific assignments of the β-methylene protons (113).

A more rigorous approach to stereospecific assignment matches the experimental intraresidue and sequential interresidue NOEs involving the NH, $C^\alpha H$, and $C^\beta H$ protons and the $^3J_{HN\alpha}$ and $^3J_{\alpha\beta}$ coupling constants with those calculated for conformations present in a data base (60, 94). The procedure is carried out for the alternative stereospecific assignments, and, if the data base contains only conformations consistent with one of the two possibilities, the correct assignment, as well as the allowed ranges for ϕ, ψ, and χ_1, can be determined. Two kinds of data bases can be used, namely a systematic data base containing the complete ϕ, ψ, and χ_1 conformational space (in e.g. 10° grid intervals) of a short tripeptide fragment with idealized geometry (60, 94) and a crystallographic data base of high resolution X-ray structures (94). Generally the stereospecific assignments obtained with both data bases are very similar, and in practice, one should evaluate the combined information extracted from both data bases (94).

Experience with this conformational data-base-search approach using both experimental data and model calculations indicates that on average one can obtain stereospecific assignments for 70–80% of the β-methylene groups (21, 60, 80, 94, 98). Further, even when no stereospecific assignment is possible, the results of the search usually contain valuable information in the form of torsion-angle restraints that are consistent with the experimental data. These ranges can also be obtained for residues with only a single β proton such as threonine, isoleucine, and valine, because the β-proton of Thr and Ile is equivalent to $\beta 2$, and that of Val to $\beta 3$.

IDENTIFICATION AND LOCALIZATION OF BOUND WATER USING HETERONUCLEAR 3D NMR METHODS

Internal bound water molecules often appear in protein X-ray structures (3). They generally either play a role in stabilizing the structure through bridging hydrogen bonding interactions or are involved in protein function. Bound water molecules can be observed with NMR by using rotating frame Overhauser (ROESY) experiments (23, 103) because interactions between the protein's protons and water arising from through-space (<4 Å) nuclear Overhauser effects and chemical exchange produce cross peaks of opposite sign (14, 40). The first observation of bound internal water was made using the 2D ^{1}H-^{1}H ROESY experiment on the small 57-residue protein bovine pancreatic trypsin inhibitor (103). Unfortunately, the application of 2D methods to the identification of bound water is very limited because extensive resonance overlap, arising from the fact that such interactions produce cross peaks on only a single trace of the 2D spectrum (parallel to the F_2 axis at the F_1 frequency of the H_2O resonance), prevents interpretation of the results.

The limitations of the 2D ROESY experiment can be completely circumvented by recording a 3D ^{1}H-^{15}N ROESY-HMQC spectrum in which ROE and chemical exchange peaks are separated out into a third dimension on the basis of the ^{15}N chemical shift of the nitrogens bonded to protons (23). The pulse scheme is depicted in Figure 4*c*. Although this sequence is similar to the ^{1}H-^{15}N HOHAHA-HMQC sequence, it contains a number of differences that permit the suppression of the water resonance without perturbing the observation of ROE effects between water and ^{15}N-bound protons.

Figure 10 illustrates the application of the 3D ^{1}H-^{15}N ROESY-HMQC experiment to ^{15}N-labeled IL-1β. The figure shows four slices at different ^{15}N chemical shifts of the 3D ^{1}H-^{15}N ROESY-HMQC spectrum of ^{15}N-labeled IL-1β (23). Fifteen cross peaks that could be unambiguously attributed to ROEs between NH protons and water were identified in the complete spectrum. Examination of the crystal structure of IL-1β (51) revealed that these NH protons are very close to 11 water molecules involved in hydrogen bonding interactions with backbone amide and carbonyl groups, stabilizing the threefold pseudosymmetric topology of IL-1β (45, 51). These bound water molecules thus constitute an integral part of the protein structure in solution (23).

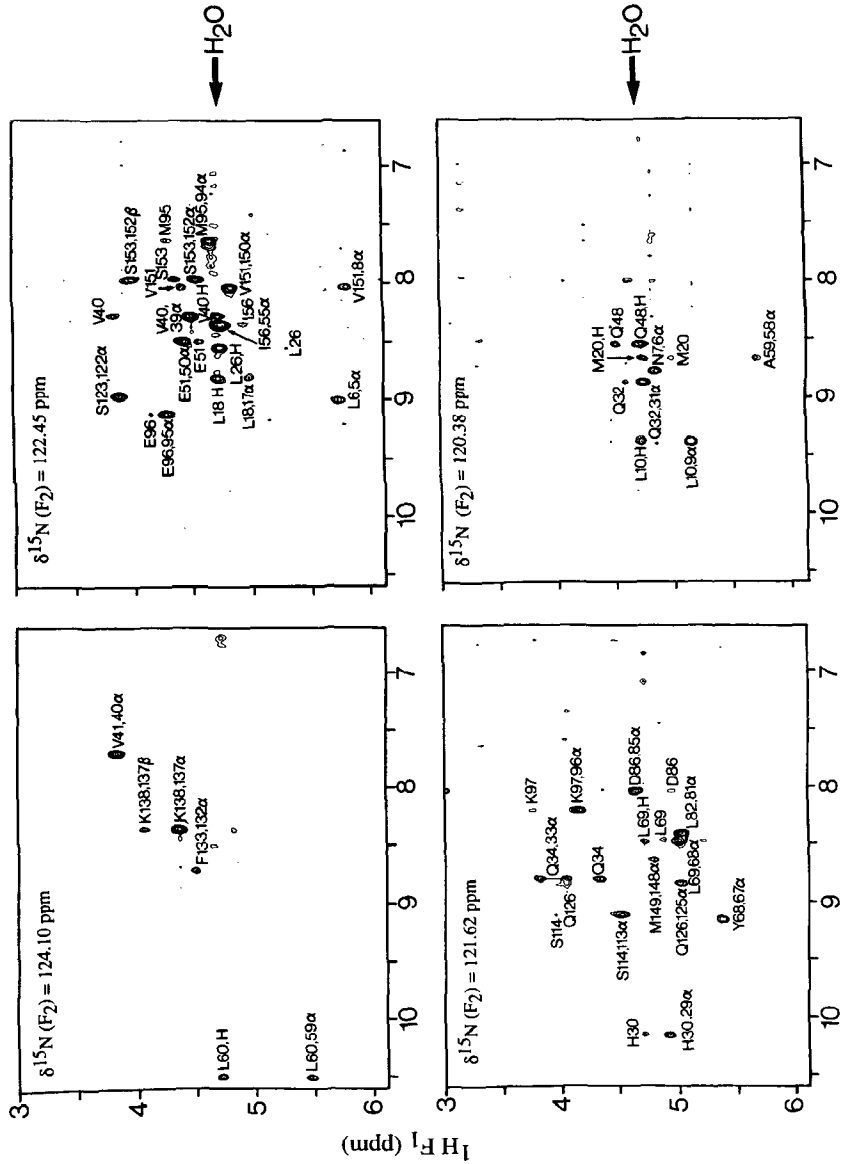

Figure 10 Selected NH(F_3)-^{1}H(F_1) planes at different ^{15}N(F_2) frequencies of the ^{1}H-^{15}N ROESY-HMQC spectrum of ^{15}N-labeled IL-1β illustrating rotating frame through-space Overhauser effects (ROE) between NH protons and bound water. Reprinted with permission from Reference 23.

COMPUTATION OF THREE-DIMENSIONAL STRUCTURES ON THE BASIS OF NMR DATA

Two main classes of methods for determining 3D structures from interproton distance restraints can be used to efficiently sample the conformational space consistent with the experimental data in an unbiased manner: (*a*) distance space methods and (*b*) real space methods. Because several reviews have covered these in detail (15, 28, 34, 62), we discuss only the key elements in this section. Distance space methods involve the application of metric matrix distance geometry, a technique used to project a set of distances from *n*-dimensional space into three-dimensional cartesian coordinate space (62). (Note the cartesian coordinates are given by the eigenvalues of the distance matrix.) Real space methods, on the other hand, operate directly in either cartesian coordinate space or torsion-angle space and involve the application of minimization (12, 17) or molecular dynamics (19, 24, 30, 69, 92, 93, 95, 96).

All methods seek to locate the global minimum region of a target function made up of the sum of empirical and experimental NMR terms. Covalent (bonds, angles, planes, and chirality) and nonbonded terms make up the empirical portion. The nonbonded term may be represented either by a simple van der Waals repulsion potential or alternatively by a full empirical energy term comprising a 6–12 Lennard-Jones van der Waals potential that has a repulsive and attractive component, an electrostatic potential, and a hydrogen bonding potential (71). Although the latter representation of the nonbonding interactions more closely approximates reality than a simple van der Waals repulsion term, the choice of nonbonding potential in the case of proteins is not critical because many tertiary NOEs between residues far apart in the sequence define the polypeptide fold (28). For oligonucleotides, however, a full representation of the van der Waals term is important because NOEs are only observed between adjacent base pairs (58, 96). The use of a full nonbonded energy function, however, does not provide the driving force for the structural changes that occur but simply ensures near optimal stereochemistry and van der Waals contacts of the resulting structures (58).

The experimental NMR term, F_{NMR}, consists of the sum of interproton-distance ($F_{H\text{-}H}$) and torsion-angle (F_{tor}) restraints, usually in the form of square-well potentials (17, 35, 63). In the interproton-distance restraints, the lower limit is usually set to 1.8 Å (i.e. the sum of the van der Waals radii of two protons) and the upper limits are classified into three (or sometimes four) ranges, for example <2.7 Å, <3.3 Å, and <5.0 Å, corresponding to strong, medium, and weak NOEs, respectively (35, 114). Whilst more accurate interproton distance restraints could in principle be obtained

from a complete relaxation matrix analysis of the NOE data (13), this analysis is often frought with difficulties owing to the very poor determination of small direct cross-relaxation rates in relaxation pathways dominated by indirect cross relaxation (29) and to differential internal motion that may attenuate the observed NOEs (25, 37). Further, as is shown below, sufficiently precise structures can be obtained simply by using many approximate interproton distance restraints, without recourse to accurate distances, thereby avoiding any complications arising from the influence of internal motions on the magnitude of the NOEs (21, 80, 98, 106).

A completed structure determination necessarily includes an assessment of the structures, which should be based on the following three criteria. First, the experimental interproton distance and torsion angle restraints must be satisfied within the errors of the experimental data. Second, the deviation from idealized covalent geometry should be very small. Third, the nonbonded contacts should be good. The quality of the contacts can be evaluated by computing the Lennard-Jones van der Waals energy (E_{LJ}) of the structures (28). This energy is very sensitive to bad contacts. For a good structure, E_{LJ} will be negative. In the presence of even minimally bad contacts, E_{LJ} becomes positive. When one employs a target function with a simple van der Waals repulsion term (17, 63, 92, 93, 95), E_{LJ} provides an independent test because the Lennard-Jones van der Waals potential is not used to calculate structures.

Finally, the precision of the structures must be evaluated. To this end, numerous structures (at least 20) are calculated using different starting conformations and different random number seeds. The spread observed in a best-fit superposition of all the calculated structures and a plot of the atomic rms distribution with respect to the mean then allows one to qualitatively and quantitatively assess, respectively, the precision associated with different regions of the protein (28).

EXAMPLES OF THREE-DIMENSIONAL PROTEIN STRUCTURES DETERMINED BY NMR

The attainable precision of a protein-structure determination depends crucially on extracting as many approximate interproton distance (<5 Å) and torsion angle restraints as possible from the experimental data. Extremely good definition of the atomic positions can be achieved using NOE interproton distance restraints classified into only three (or four) broad distance ranges (e.g. ≤ 2.7, ≤ 3.3, and ≤ 5.0 Å), thus avoiding any potential problems associated with variable internal mobility and r^{-6} averaging. These results are due to the fact that many of the interproton

distances are highly correlated and short (< 5 Å) distances between residues far apart in the sequence are highly conformationally restrictive even if they are only approximate.

Illustration of Factors Affecting the Precision and Accuracy of a Protein-Structure Determination by NMR

Figure 11 illustrates the progressive improvement in structural precision attainable by increasing the number of approximate interproton-distance and torsion-angle restraints. In each case, the interproton-distance restraints used are only approximate and classified into the three broad ranges described above. The first structure displayed is that of phoratoxin (36) (Figure 11*A*), a small 46-residue protein that is a member of a ubiquitous class of toxins throughout the plant kingdom. The structure is based on 331 approximate interproton distance restraints alone and represents an example of what can be termed a first-generation NMR structure. The atomic rms distribution about the mean coordinate positions is 1.7 ± 0.5 Å for the backbone atoms and 2.1 ± 0.5 Å for all atoms. Other first-generation structures of similar quality include, for example, proteinase inhibitor IIA from bull seminal plasma inhibitor (114), purothionin (35), lac repressor headpiece (69), the globular domain of histone H5 (33), bovine pancreatic trypsin inhibitor (113), human epidermal

Figure 11 Illustration of the progressive improvement in the precision and accuracy of NMR structure determinations obtained by increasing the number of experimental restraints. (*A*) Best superposition of the backbone atoms of 8 restrained molecular dynamics structures of phoratoxin (46 residues) calculated on the basis of 331 interproton distance restraints; (*B*) best-fit superposition of the backbone and representative side chains of 31 simulated annealing structures of BDS (43 residues) calculated on the basis of 409 interproton-distance restraints (with no stereospecific assignments) together with distance restraints for 12 hydrogen bonds and 23 ϕ backbone torsion-angle restraints derived from $^3J_{HN\alpha}$ coupling constants; (*C*) best-fit superposition of the backbone and representative side chains of 42 simulated annealing structures of BDS calculated on the basis of 489 interproton-distance restraints (including stereospecific assignments for 19 out of 30 β-methylene groups) supplemented by distance restraints for 12 hydrogen bonds and 23 ϕ and 21 χ_1 side-chain torsion-angle restraints derived from a qualitative analysis of the intraresidue NOE and coupling-constant data; (*D*) best-fit superposition of the backbone atoms and representative side chains of the 41 simulated annealing structures of the C-terminal domain of cellobiohydrolase I (36 residues) determined on the basis of 554 interproton-distance restraints (including stereospecific assignments for 17 out of 22 β-methylene groups), restraints for 12 hydrogen bonds, and 33 ϕ, 24 ψ, and 25 χ_1 torsion-angle restraints obtained using a data-base-search procedure on the basis of NOE and coupling constant data. The structures in *A*, *B*, *C*, and *D* correspond to what can be termed first-, second-, third-, and fourth-generation NMR structures, respectively. In all these examples, the interproton-distance restraints have only been classified into three broad ranges, ≤ 2.7 Å, ≤ 3.3 Å, and ≤ 5.0 Å, corresponding to strong, medium, and weak NOEs, respectively.

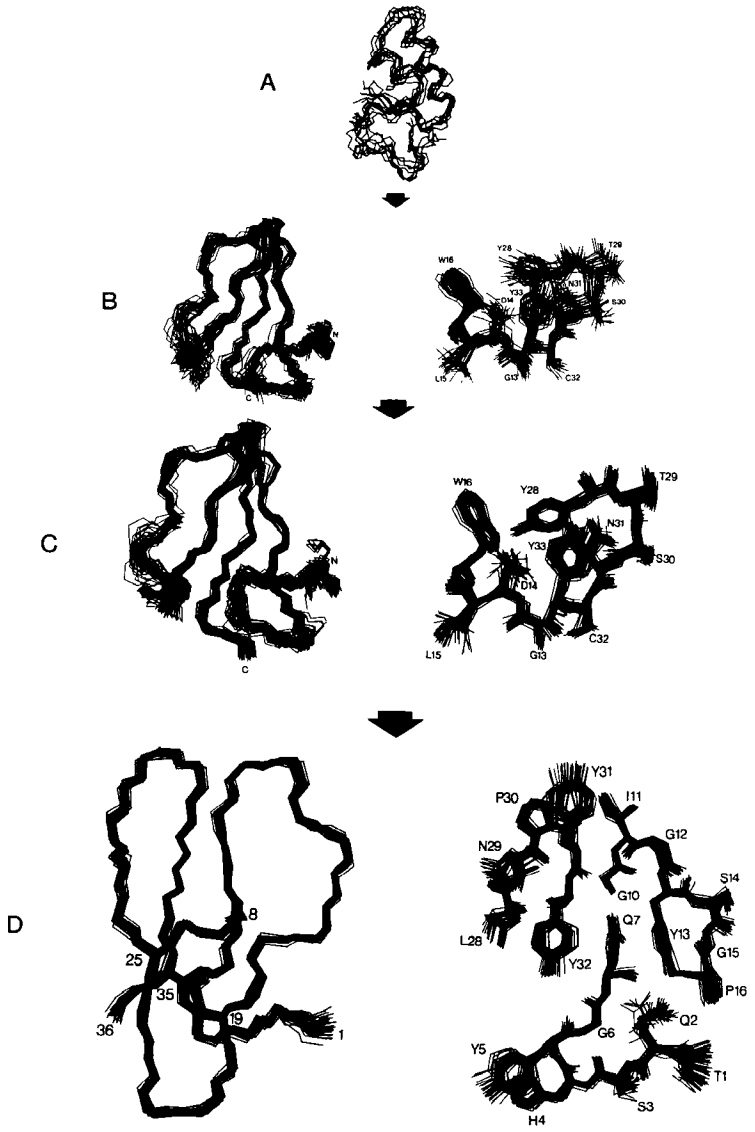

growth factor (38), potato carboxypeptidase inhibitor (32), barley serine proteinase inhibitor II (31), C5a (120), acyl carrier protein (64), rabbit neutrophil defensin NP-5 (105), acylphosphatase (108), kringle 4 (1), and a zinc-finger domain from ADR1b (78). An increase in the number of distance restraints supplemented by, if possible, a few ϕ backbone torsion-angle restraints derived from a qualitative interpretation of $^3J_{HN\alpha}$ coupling constants can significantly improve the resolution. Figure 11*B* illustrates this improvement with regard to the structure of the 43-residue protein BDS-1 from the sea anemone, determined on the basis of 409 approximate interproton-distance restraints with no stereospecific assignments but supplemented by distance restraints for 12 hydrogen bonds (obtained from a qualitative interpretation of the NOE and amide-exchange data) and 23 ϕ backbone torsion-angle restraints (derived from $^3J_{HN\alpha}$ coupling constants) (44). The atomic rms distribution about the mean in this case is 0.93 ± 0.16 Å for the backbone atoms and 1.17 ± 0.17 Å for all atoms. The structure in Figure 11*B* constitutes a second-generation NMR structure. Examples of other structures of similar quality are plastocyanin (88) and the zinc-finger domain of Xfin III (81). However, the structure is improved much more by including stereospecific assignments and some χ_1 torsion-angle restraints derived from a qualitative interpretation of the $^3J_{\alpha\beta}$ and intra-residue NOE data, as illustrated for BDS in Figure 11*C* (43). Stereospecific assignments were obtained for 19 out of the 30 β-methylene groups, and the structure is based on 489 approximate interproton-distance restraints, distance restraints for 12 hydrogen bonds, and 23 ϕ and 21 χ_1 side-chain torsion-angle restraints. (Note the latter are only restrained to $\pm 60°$ of the relevant preferred rotamer population.) The atomic rms distribution about the mean is 0.67 ± 0.12 Å for the backbone atoms and 0.90 ± 0.17 Å for all atoms. Thus, the side-chain and backbone atom positions reflect the improvement equally well. For example, in the BDS structures calculated with stereospecific assignments and χ_1 torsion-angle restraints, the presence of a hydrogen bond between the $N^{\varepsilon 1}H$ of the indole ring of Trp-16 and the hydroxyl O^{η} of Tyr-28 is clearly revealed, whereas in the structures calculated without stereospecific assignments such a conclusion cannot be drawn because of the much poorer side-chain definition (Figures 11*B* and *C*). The BDS structure calculated with stereospecific assignments and χ_1 torsion angle restraints represents a third-generation NMR structure. Other examples of third generation structures are tendamistat (79), hirudin (52, 61), and *Escherichia coli* thioredoxin (46).

The precision of the structures determined by NMR can be advanced another step using a two-pronged strategy with further improvements at both the qualitative and quantitative levels (80). First, many more stereospecific assignments as well as tighter and more numerous torsion

angle restraints can be obtained by application of the data-base procedure discussed in the section on data-base researches (60, 94). Second, one can employ an iterative strategy in the structure determination process that consists of a series of calculations with more and more restraints incorporated at each successive stage, thereby enabling one to resolve ambiguities relating not only to the assignment of some NOE cross peaks but also to stereospecific assignments. Figure 11*D* illustrates an example of a fourth-generation NMR structure determined using this approach with respect to a 36-residue polypeptide comprising the C-terminal domain of cellobiohydrolase I (80). The final experimental data set for this structure determination consisted of 554 approximate interproton-distance restraints, distance restraints for 12 hydrogen bonds, and 33 ϕ, 24 ψ, and 25 χ_1 torsion-angle restraints. (Note that torsion-angle restraints are still very conservative because the minimum deviations for the ϕ, ψ, and χ_1 angles were set to ± 30, ± 50, and $\pm 20°$, respectively, although in many cases the ranges derived from the data-base searches were smaller.) The converged set of 41 structures represent one of the best-quality NMR structures solved to date, exhibiting a backbone atomic rms distribution about the mean coordinate positions of 0.33 ± 0.04 Å for the backbone atoms and 0.52 ± 0.06 Å for all atoms. Other examples of fourth-generation structures of comparable precision and accuracy are interleukin-8 (21), a zinc-finger domain from a human enhancer binding protein (98), and the homeodomain of the Antennapedia protein (106). The overall quality of these structures is comparable to that of an $\sim$2-Å-resolution crystal structure.

The Solution Structure of Interleukin-8: A Case Study

As an example of a high-resolution fourth-generation NMR structure, we discuss the solution structure of interleukin-8 (IL-8) (21), which is a member of the cytokine family and plays a key role in the immune and inflammatory responses (85). IL-8 is a dimeric protein of 16 kd composed of two identical subunits of 72 residues each (20). Its solution structure was determined on the basis of a total of 1694 interproton distance restraints, distance restraints for 52 backbone hydrogen bonds, 362 torsion-angle restraints for the two subunits combined, and 70 interproton-distance restraints and distance restraints for 6 backbone hydrogen bonds between the subunits. Stereospecific assignments were obtained for 38 of the 55 β-methylene groups per monomer and for the α-methylene groups of the two glycine residues.

Figure 12 shows best-fit superpositions of 30 simulated annealing (SA) structures for the backbone atoms and selected side chains. The structure consists of two antiparallel α-helices lying on top of a six-stranded anti-

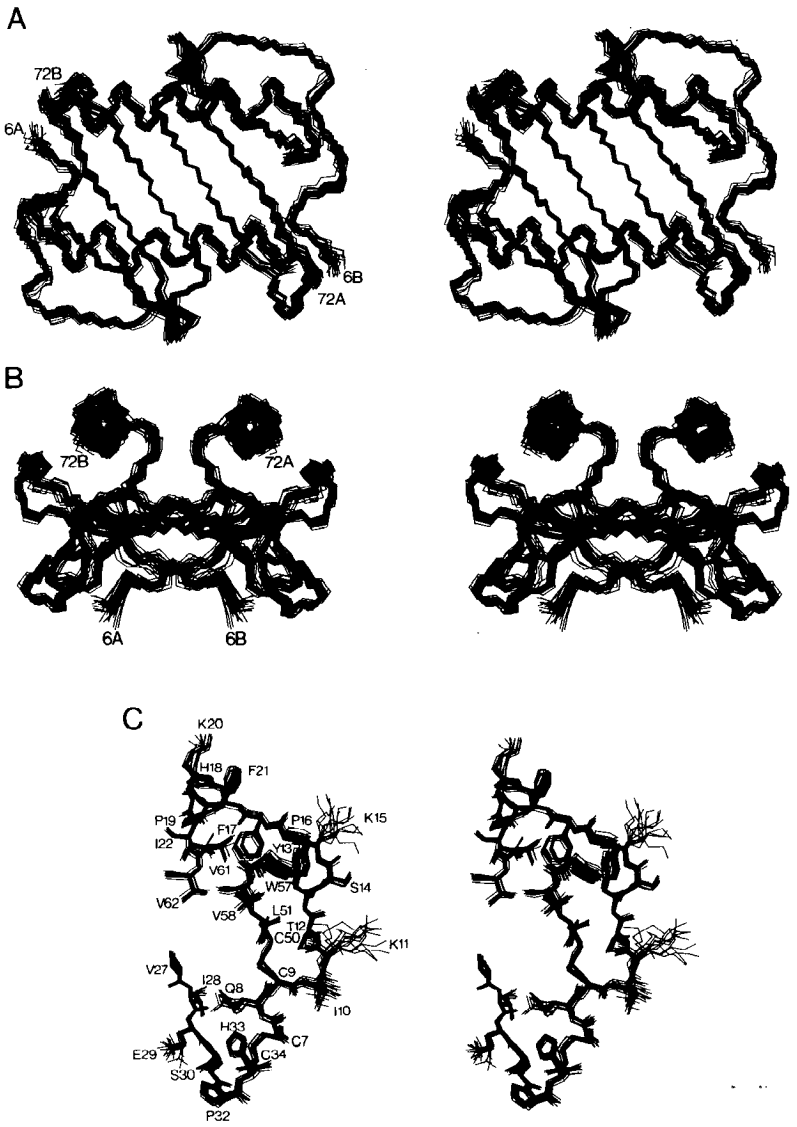

Figure 12 (*A* and *B*) Two views of best-fit superpositions of the backbone atoms of 30 simulated annealing structures of the IL-8 dimer determined on the basis of a total of 1880 approximate experimental distance restraints (of which 82 are intersubunit) and 362 torsion-angle restraints comprising ϕ, ψ, and χ_1 torsion angles; (*C*) best-fit superposition of all nonhydrogen atoms of a representative segment of IL-8 for 15 simulated annealing structures. Reprinted with permission from Reference 21.

parallel β-sheet derived from two three-stranded Greek keys, one from each monomer unit (Figure 12*A*). The surface under the β-sheet is concave and with the exception of only two residues (Ile-28 and Ile-40) is composed entirely of hydrophilic and charged residues (Figure 12*B*). The two-symmetry related helices, $\sim$24 Å in length, are positioned at an angle of about $+60°$ with respect to the orientation of the β-strands and separated by a center-to-center distance of $\sim$14 Å. This general architecture is similar to that of the α1-α2 domains of the human class I histocompatibility antigen HLA-A2 in which the sheet is formed by eight β-strands, four from each domain, with two helices separated by $\sim$18 Å running across them at an angle of about $-45°$.

Except for residues 1–5, which have a random conformation in solution, the structure is exceptionally well determined. It has an atomic rms distribution about the mean coordinate positions of 0.41 ± 0.08 Å for the backbone atoms and 0.90 ± 0.08 Å for all atoms. The average angular rms difference for the ϕ and ψ torsion angles is $8.7 \pm 5.9°$, and the backbone torsion angles for all nonglycine residues lie in the allowed region of the Ramachandran ϕ, ψ plot. The internal side chains in the IL-8 structure are also well defined and have atomic rms distributions about the mean coordinate positions of $\leq$0.5 Å (Figure 12*C*). Eighteen side chains, however, have atomic rms distributions about the mean coordinate positions larger than 1 Å. All of these residues are highly surface accessible, and the $^3J_{\alpha\beta}$ coupling constants indicate multiple χ_1 side chain conformations.

Subsequent to the NMR structure determination, the X-ray structure of IL-8 at 1.5 Å was solved by molecular replacement using the solution structure as a model (4). Although researchers had previously shown that NMR structures could be used as a basis for molecular replacement (16, 18), IL-8 represents the first example of a solution for a crystal structure that necessitated using a NMR structure because suitable heavy-atom derivatives could not be obtained to solve the phase problem with isomorphous replacement.

CONCLUDING REMARKS

Since the publication of the first NMR protein structures several years ago, the methodology and its application have made tremendous strides forward. The first-generation NMR structures were of low resolution and provided a global description of the polypeptide fold (35, 114). In contrast, the fourth-generation structures now attainable are of high resolution and comparable in quality to $\sim$2-Å-resolution crystal structures (21, 80, 98, 106). Noteworthy in this respect is the fact that such structures can be obtained by using only approximate and very generous interproton-dis-

tance restraints, supplemented by stereospecific assignments and loose ϕ, ψ, and χ_1 torsion-angle restraints. Similarly, improvements with respect to the size of the proteins that can be tackled using the NMR approach have occurred at an ever increasing pace, most notably within the past year, which has seen heteronuclear techniques employed, in particular those that use 3D and 4D NMR spectroscopy and uniformly enriched (>95%) ^{15}N- and/or ^{13}C-labeled proteins. Thus, although structure determinations on proteins of 50–60 residues constituted a major effort only very recently, we can currently tackle proteins of up to 20–25 kd and 150–200 residues. In this regard, the 3D heteronuclear NMR studies on IL-1β (153 residues) presents the first published example of a protein of this size for which complete ^{1}H, ^{15}N, and ^{13}C assignments have been obtained (22, 42), the secondary structure elucidated (45), and low-resolution three-dimensional structure determined (26). Similar studies on calmodulin (65, 67), T4 lysozyme (48, 119), and Staphylococcal nuclease (84) are currently in progress.

The next few years will most likely see many further developments in NMR methodology, relating to increases in dimensionality of the basic NMR experiment (of which 4D NMR is an example), improved data processing procedures such as the appropriate use of linear prediction, and advanced procedures for NMR data analysis and interpretation. In this regard, the immense spectral simplification that accompanies the large increase in resolution afforded by 3D and 4D NMR methods should permit the development of near-automated procedures for spectral assignment and NOE identification, thereby considerably speeding up the process of structure determination of larger proteins in solution. But most importantly, we will see many more actual examples of high resolution protein structures determined by NMR, thereby increasing our knowledge base of protein architecture and adding to the enormously useful pool of available structures for correlation with functional properties.

Acknowledgments

We thank our colleagues who have participated in various aspects of the work described in this review for many fruitful collaborations and stimulating discussions, in particular Ettore Appella, Ad Bax, Axel Brünger, Paul Driscoll, Julie Forman-Kay, Lewis Kay, Dominique Marion, Michael Nilges, Jim Omichinski, Attila Szabo, Rolf Tschudin, and Paul Wingfield. The work in the authors' laboratory was supported in part by a grant from the Intramural AIDS Directed Anti-Viral Program of the Office of the Director of the National Institutes of Health.

Literature Cited

1. Atkinson, R. A., Williams, R. J. P. 1990. *J. Mol. Biol.* 21: 541–52
2. Aue, W. P., Bartholdi, E., Ernst, R. R. 1976. *J. Chem. Phys.* 64: 2229–46
3. Baker, E., Hubbard, R. 1984. *Prog. Biophys. Mol. Biol.* 44: 97–79
4. Baldwin, L., Weber, I. T., St. Charles, R., Cheng, J. C., Appella, E., et al. 1990. *Proc. Natl. Acad. Sci. USA.* In press
5. Bax, A. 1989. *Annu. Rev. Biochem.* 58: 223–56
6. Bax, A. 1989. *Methods Enzymol.* 176: 151–68
7. Bax, A., Clore, G. M., Driscoll, P. C., Gronenborn, A. M., Ikura, M., Kay, L. E. 1990. *J. Magn. Reson.* 87: 620–28
8. Bax, A., Clore, G. M., Gronenborn, A. M. 1990. *J. Magn. Reson.* 88: 425–31
9. Bax, A., Freeman, R. 1981. *J. Magn. Reson.* 45: 177–81
10. Bax, A., Griffey, R. H., Hawkins, B. L. 1983. *J. Magn. Reson.* 55: 301–15
11. Bax, A., Weiss, M. 1987. *J. Magn. Reson.* 71: 571–75
12. Billeter, M., Havel, T. F., Wüthrich, K. 1987. *J. Comput. Chem.* 8: 132–41
13. Borgias, B., Gochin, M., Kerwood, D. J., James, T. L. 1990. *Prog. Nucl. Magn. Reson. Spectrosc.* 22: 83–100
14. Bothner-By, A. A., Stephens, R. L., Lee, J. T., Warren, C., Jeanloz, R. W. 1984. *J. Am. Chem. Soc.* 106: 811–13
15. Braun, W. 1987. *Q. Rev. Biophys.* 19: 115–57
16. Braun, W., Epp, O., Wüthrich, K., Huber, R. 1989. *J. Mol. Biol.* 206: 669–76
17. Braun, W., Go, N. 1985. *J. Mol. Biol.* 186: 611–26
18. Brünger, A. T., Campbell, R. L., Clore, G. M., Gronenborn, A. M., Karplus, M., et al. 1987. *Science* 235: 1049–53
19. Brünger, A. T., Clore, G. M., Gronenborn, A. M., Karplus, M. 1986. *Proc. Natl. Acad. Sci. USA* 83: 3801–3905
20. Clore, G. M., Appella, E., Yamada, E., Matsushima, K., Gronenborn, A. M. 1989. *J. Biol. Chem.* 264: 18907–11
21. Clore, G. M., Appella, E., Yamada, E., Matsushima, K., Gronenborn, A. M. 1990. *Biochemistry* 29: 1689–96
22. Clore, G. M., Bax, A., Driscoll, P. C., Wingfield, P. T., Gronenborn, A. M. 1990. *Biochemistry* 29: 8172–84
23. Clore, G. M., Bax, A., Wingfield, P. T., Gronenborn, A. M. 1990. *Biochemistry* 29: 5671–76
24. Clore, G. M., Brünger, A. T., Karplus, M., Gronenborn, A. M. 1986. *J. Mol. Biol.* 191: 523–51
25. Clore, G. M., Driscoll, P. C., Wingfield, P. T., Gronenborn, A. M. 1990. *Biochemistry* 29: 7387–7401
26. Clore, G. M., Driscoll, P. C., Wingfield, P. T., Gronenborn, A. M. 1990. *J. Mol. Biol.* 214: 811–17
27. Clore, G. M., Gronenborn, A. M. 1987. *Protein Eng.* 1: 275–88
28. Clore, G. M., Gronenborn, A. M. 1989. *CRC Crit. Rev. Biochem. Mol. Biol.* 24: 479–564
29. Clore, G. M., Gronenborn, A. M. 1989. *J. Magn. Reson.* 84: 398–409
30. Clore, G. M., Gronenborn, A. M., Brünger, A. T., Karplus, M. 1985. *J. Mol. Biol.* 186: 435–55
31. Clore, G. M., Gronenborn, A. M., Kjaer, M., Poulsen, F. M. 1987. *Protein Eng.* 1: 305–11
32. Clore, G: M., Gronenborn, A. M., Nilges, M., Ryan, C. A. 1987. *Biochemistry* 26: 8012–23
33. Clore, G. M., Gronenborn, A. M., Nilges, M., Sukumaran, D. K., Zarbock, J. 1987. *EMBO J.* 6: 1833–42
34. Clore, G. M., Nilges, M., Gronenborn, A. M. 1989. In *Computer-Aided Molecular Design*, ed. W. G. Richards, pp. 203–19. London: IBC Technical Services
35. Clore, G. M., Nilges, M., Sukumaran, D. K., Brünger, A. T., Karplus, M., Gronenborn, A. M. 1986. *EMBO J.* 5: 2729–35
36. Clore, G. M., Sukumaran, D. K., Nilges, M., Gronenborn, A. M. 1987. *Biochemistry* 26: 1732–45
37. Clore, G. M., Szabo, A., Bax, A., Kay, L. E., Driscoll, P. C., Gronenborn, A. M. 1990. *J. Am. Chem. Soc.* 112: 4989–91
38. Cooke, R. M., Wilkinson, A. J., Baron, M., Pastore, A., Tappin, M. J., et al. 1987. *Nature* (*London*) 327: 339–41
39. Davis, D. G., Bax, A. 1985. *J. Am. Chem. Soc.* 107: 2820–21
40. Davis, D. G., Bax, A. 1985. *J. Magn. Reson.* 64: 533–35
41. DeMarco, A., Llinas, M., Wüthrich, K. 1978. *Biopolymers* 17: 617–36
42. Driscoll, P. C., Clore, G. M., Marion, D., Wingfield, P. T., Gronenborn, A. M. 1990. *Biochemistry* 29: 3542–56
43. Driscoll, P. C., Gronenborn, A. M., Beress, L., Clore, G. M. 1989. *Biochemistry* 28: 2188–98
44. Driscoll, P. C., Gronenborn, A. M., Clore, G. M. 1989. *FEBS Lett.* 243: 223–33
45. Driscoll, P. C., Gronenborn, A. M., Wingfield, P. T., Clore, G. M. 1990. *Biochemistry* 29: 4668–82

46. Dyson, H. J., Gippert, G. P., Case, D. A., Holmgren, A., Wright, P. E. 1990. *Biochemistry* 29: 4129–36
47. Ernst, R. R., Bodenhausen, G., Wokaun, A. 1987. *Principles of Nuclear Magnetic Resonance in One and Two Dimensions*. Oxford: Clarendon
48. Fesik, S. W., Eaton, H. L., Olejniczak, E. T., Zuiderweg, E. R. P., McIntosh, L. P., Dahlquist, F. W. 1990. *J. Am. Chem. Soc.* 112: 886–87
49. Fesik, S. W., Gampe, R. T., Rockway, T. W. 1987. *J. Magn. Reson.* 74: 366–71
50. Fesik, S. W., Zuiderweg, E. R. P. 1988. *J. Magn. Reson.* 78: 588–93
51. Finzel, B. C., Clancy, L. L., Holland, D. R., Muchmore, S. W., Watenpaugh, K. D., Einspahr, H. M. 1989. *J. Mol. Biol.* 209: 779–91
52. Folkers, P. J. M., Clore, G. M., Driscoll, P. C., Dodt, J., Köhler, S., Gronenborn, A. M. 1989. *Biochemistry* 28: 2601–17
53. Forman-Kay, J. D., Gronenborn, A. M., Kay, L. E., Wingfield, P. T., Clore, G. M. 1990. *Biochemistry* 29: 1566–72
54. Griesinger, C., Sørensen, O. W., Ernst, R. R. 1982. *J. Am. Chem. Soc.* 104: 6800–2
55. Griesinger, C., Sørensen, O. W., Ernst, R. R. 1987. *J. Magn. Reson.* 73: 574–79
56. Griffey, R. G., Redfield, A. G. 1987. *Q. Rev. Biophys.* 19: 51–82
57. Gronenborn, A. M., Bax, A., Wingfield, P. T., Clore, G. M. 1989. *FEBS Lett.* 243: 93–98
58. Gronenborn, A. M., Clore, G. M. 1989. *Biochemistry* 28: 5978–84
59. Gronenborn, A. M., Clore, G. M. 1990. *Anal. Chem.* 62: 2–15
60. Güntert, P., Braun, W., Billeter, M., Wüthrich, K. 1989. *J. Am. Chem. Soc.* 111: 3997–4004
61. Haruyama, H., Wüthrich, K. 1989. *Biochemistry* 28: 4301–12
62. Havel, T. F., Kuntz, I. D., Crippen, G. M. 1983. *Bull. Math. Biol.* 45: 665–720
63. Havel, T. F., Wüthrich, K. 1984. *Bull. Math. Biol.* 46: 673–98
64. Holak, T. A., Nilges, M., Prestegard, J. H., Gronenborn, A. M., Clore, G. M. 1988. *Eur. J. Biochem.* 175: 9–15
65. Ikura, M., Kay, L. E., Bax, A. 1990. *Biochemistry* 29: 4659–67
66. Ikura, M., Kay, L. E., Tschudin, R., Bax, A. 1990. *J. Magn. Reson.* 86: 204–9
67. Ikura, M., Marion, D., Kay, L. E., Shih, H., Krinks, M., et al. 1990. *Biochem. Pharmacol.* 40: 153–60
68. Jeener, J., Meier, B. H., Bachman, P., Ernst, R. R. 1979. *J. Chem. Phys.* 71: 4546–53
69. Kaptein, R., Zuiderweg, E. R. P., Scheek, R., Boelens, R., van Gunsteren, W. F. 1985. *J. Mol. Biol.* 182: 179–82
70. Karplus, M. 1963. *J. Am. Chem. Soc.* 85: 2870–71
71. Karplus, M., McCammon, J. A. 1983. *Annu. Rev. Biochem.* 52: 263–300
72. Kay, L. E., Bax, A. 1990. *J. Magn. Reson.* 86: 110–26
73. Kay, L. E., Brooks, B., Sparks, S. W., Torchia, D. A., Bax, A. 1989. *J. Am. Chem. Soc.* 111: 1515–16
74. Kay, L. E., Clore, G. M., Bax, A., Gronenborn, A. M. 1990. *Science* 249: 411–14
75. Kay, L. E., Ikura, M., Bax, A. 1990. *J. Am. Chem. Soc.* 112: 888–89
76. Kay, L. E., Ikura, M., Tschudin, R., Bax, A. 1990. *J. Magn. Reson.* 89: 496–514
77. Kay, L. E., Marion, D., Bax, A. 1989. *J. Magn. Reson.* 84: 72–84
78. Klevitt, R. E., Herriot, J. R., Horwarth, S. W. 1990. *Proteins: Struc. Funct. and Genet.* 7: 215–26
79. Kline, A. D., Braun, W., Wüthrich, K. 1988. *J. Mol. Biol.* 204: 675–724
80. Kraulis, P. J., Clore, G. M., Nilges, M., Jones, T. A., Pettersson, G., et al. 1989. *Biochemistry* 28: 7241–57
81. Lee, M. S., Gippert, G. P., Soman, K. V., Case, D. A., Wright, P. E. 1989. *Science* 245: 635–37
82. Marion, D., Bax, A. 1988. *J. Magn. Reson.* 80: 528–33
83. Marion, D., Driscoll, P. C., Kay, L. E., Wingfield, P. T., Bax, A., et al. 1989. *Biochemistry* 29: 6150–56
84. Marion, D., Kay, L. E., Sparks, S. W., Torchia, D. A., Bax, A. 1989. *J. Am. Chem. Soc.* 111: 1515–17
85. Matsushima, K., Oppenheim, J. J. 1989. *Cytokine* 1: 2–13
86. McIntosh, L. P., Dahlquist, F. W., Redfield, A. G. 1987. *J. Biomol. Struc. Dyn.* 5: 21–34
87. McIntosh, L. P., Griffey, R. H., Muchmore, D. C., Nielson, C. P., Redfield, A. G., Dahlquist, F. W. 1987. *Proc. Natl. Acad. Sci. USA* 84: 1244–48
88. Moore, J. M., Case, D. A., Chazin, W. J., Gippert, G. P., Havel, T. F., et al. 1988. *Science* 240: 314–17
89. Mueller, L. 1979. *J. Am. Chem. Soc.* 101: 4481–84
90. Mueller, L. 1987. *J. Magn. Reson.* 72: 191–96
91. Neuhaus, D., Wagner, G., Vasak, K., Kägi, J. H. R., Wüthrich, K. 1985. *Eur. J. Biochem.* 151: 257–73

92. Nilges, M., Clore, G. M., Gronenborn, A. M. 1988. *FEBS Lett.* 229: 317–24
93. Nilges, M., Clore, G. M., Gronenborn, A. M. 1988. *FEBS Lett.* 239: 129–36
94. Nilges, M., Clore, G. M., Gronenborn, A. M. 1990. *Biopolymers* 29: 813–22
95. Nilges, M., Gronenborn, A. M., Brünger, A. T., Clore, G. M. 1988. *Protein Engin.* 2: 27–38
96. Nilsson, L., Clore, G. M., Gronenborn, A. M., Brünger, A. T., Karplus, M. 1986. *J. Mol. Biol.* 188: 455–75
97. Noggle, J. H., Schirmer, R. G. 1971. *The Nuclear Overhauser Effect.* New York: Academic
98. Omichinski, J. G., Clore, G. M., Appella, E., Sakaguchi, K., Gronenborn, A. M. 1990. *Biochemistry* 29: 9324–34
99. Oschkinat, H., Cieslar, C., Gronenborn, A. M., Clore, G. M. 1989. *J. Magn. Reson.* 81: 212–16
100. Oschkinat, H., Cieslar, C., Holak, T. A., Clore, G. M., Gronenborn, A. M. 1989. *J. Magn. Reson.* 83: 450–72
101. Oschkinat, H., Griesinger, C., Kraulis, P. J., Sørensen, O. W., Ernst, R. R., et al. 1988. *Nature* (*London*) 332: 374–77
102. Oschkinat, H., Pastore, A., Pfändler, P., Bodenhausen, G. 1986. *J. Magn. Reson.* 69: 559–66
103. Otting, G., Wüthrich, K. 1989. *J. Am. Chem. Soc.* 111: 1871–75
104. Pardi, A., Billeter, M., Wüthrich, K. 1984. *J. Mol. Biol.* 180: 741–51
105. Pardi, A., Hare, D. R., Selsted, M. E., Morrison, R. D., Bassolino, D. A., Bach, A. C. 1988. *J. Mol. Biol.* 201: 625–36
106. Qian, Y. Q., Billeter, M., Otting, G., Müller, M., Gehring, W. J., Wüthrich, K. 1989. *Cell* 59: 573–80
107. Redfield, A. G. 1983. *Chem. Phys. Lett.* 96: 537–40
108. Saudek, V., Williams, R. J. P., Ramponi, G. 1989. *FEBS Lett.* 242: 225–32
109. Torchia, D. A., Sparks, S. W., Bax, A. 1988. *Biochemistry* 27: 5135–41
110. Torchia, D. A., Sparks, S. W., Bax, A. 1989. *Biochemistry* 28: 5509–24
111. Vuister, G. W., Boelens, R., Kaptein, R. 1988. *J. Magn. Reson.* 80: 176–85
112. Vuister, G. W., Boelens, R., Padilla, A., Kleywegt, G. J., Kaptein, R. 1990. *Biochemistry* 29: 1829–39
113. Wagner, G., Braun, W., Havel, T. F., Schaumann, T., Go, N., Wüthrich, K. 1987. *J. Mol. Biol.* 196: 611–39
114. Williamson, M. P., Havel, T. F., Wüthrich, K. 1985. *J. Mol. Biol.* 182: 295–315
115. Wüthrich, K. 1986. *NMR of Proteins and Nucleic Acids.* New York: Wiley
116. Wüthrich, K. 1989. *Acc. Chem. Res.* 22: 36–44
117. Wüthrich, K., Billeter, M., Braun, W. 1983. *J. Mol. Biol.* 169: 949–61
118. Zuiderweg, E. R. P., Fesik, S. W. 1989. *Biochemistry* 28: 2387–91
119. Zuiderweg, E. R. P., McIntosh, L. P., Dahlquist, F. W., Fesik, S. W. 1990. *J. Magn. Reson.* 86: 210–16
120. Zuiderweg, E. R. P., Nettesheim, D. G., Mollison, K. W., Carter, C. W. 1989. *Biochemistry* 28: 172–85

Annual Review of Biophysics and Biophysical Chemistry
Volume 20, 1991

CONTENTS

(*continued*)